

AD-A269 087



2

PL-TR-93-2069

**THE USE OF VELOCITY SPECTRA FOR STACKING
RECEIVER FUNCTIONS WITH APPLICATION TO
IRIS/IDA STATIONS OBNINSK (OBN) AND ARTI
(ARU), RUSSIA**

H. Gurrola
J. B. Minster
T. Owens
H. Given

University of California, San Diego
Institute of Geophysics and Planetary Physics
9500 Gilman Drive
La Jolla, CA 92093-0225

30 October 1992

Final Technical Report covering
1 December 1991 - 30 October 1992

DTIC
SELECTE
AUG 04 1993
S B D

APPROVED FOR PUBLIC RELEASE; DISTRIBUTION UNLIMITED



PHILLIPS LABORATORY
Directorate of Geophysics
AIR FORCE MATERIEL COMMAND
HANSCOM AFB, MA 01731-3010

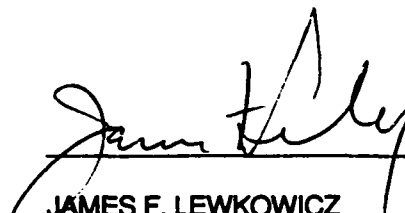
93-17458



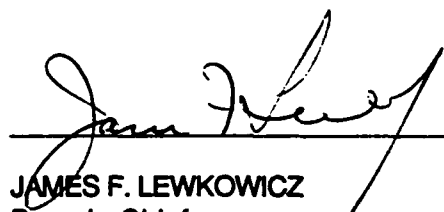
93 8 3 1 6 6

The views and conclusions contained in this document are those of the authors and should not be interpreted as representing the official policies, either expressed or implied, of the Air Force or the U.S. Government.

This technical report has been reviewed and is approved for publication.



JAMES F. LEWKOWICZ
Contract Manager
Solid Earth Geophysics Branch
Earth Sciences Division



JAMES F. LEWKOWICZ
Branch Chief
Solid Earth Geophysics Branch
Earth Sciences Division



DONALD H. ECKHARDT, Director
Earth Sciences Division

This document has been reviewed by the ESD Public Affairs Office (PA) and is releasable to the National Technical Information Service (NTIS).

Qualified requestors may obtain additional copies from the Defense Technical Information Center. All others should apply to the National Technical Information Service.

If your address has changed, or if you wish to be removed from the mailing list, or if the addressee is no longer employed by your organization, please notify PL/TSI, Hanscom AFB MA 01731-3010. This will assist us in maintaining a current mailing list.

Do not return copies of this report unless contractual obligations or notices on a specific document requires that it be returned.

REPORT DOCUMENTATION PAGE

Form Approved
OMB No. 0704-0188

Public reporting burden for this collection of information is estimated to average 1 hour per response, including the time for reviewing instructions, searching existing data sources, gathering and maintaining the data needed, and completing and reviewing the collection of information. Send comments regarding this burden estimate or any other aspect of this collection of information, including suggestions for reducing this burden, to Washington Headquarters Services, Directorate for Information Operations and Reports, 1215 Jefferson Davis Highway, Suite 1204, Arlington, VA 22202-4302, and to the Office of Management and Budget, Paperwork Reduction Project (0704-0188), Washington, DC 20503

1. AGENCY USE ONLY (Leave blank)		2. REPORT DATE October 30, 1992	3. REPORT TYPE AND DATES COVERED Final Dec. 1, 1991-Oct. 30, 1992	
4. TITLE AND SUBTITLE The Use of Velocity Spectra for Stacking Receiver Functions with Application to IRIS/IDA Stations Obninsk (OBN) and Arti (ARU), Russia		5. FUNDING NUMBERS C-F19628-90-K-0045 PE62101F PR7600 TA09 WURD		
6. AUTHOR(S) H. Gurrola, J.B. Minster, T. Owens*, and H. Given		7. PERFORMING ORGANIZATION NAME(S) AND ADDRESS(ES) Institute of Geophysics and Planetary Physics University of California, San Diego 9500 Gilman Drive La Jolla, CA 92093-0225		
8. PERFORMING ORGANIZATION REPORT NUMBER		9. SPONSORING/MONITORING AGENCY NAME(S) AND ADDRESS(ES) Phillips Laboratory 29 Randolph Road Hanscom AFB, MA 01731-3010 Contract Manager: James Lewkowicz/GPEH		
10. SPONSORING/MONITORING AGENCY REPORT NUMBER PL-TR-93-2069		11. SUPPLEMENTARY NOTES *University of South Carolina, Dept. of Geological Science Columbia, SC 29208		
12a. DISTRIBUTION/AVAILABILITY STATEMENT approved for public release: distribution unlimited		12b. DISTRIBUTION CODE		
13. ABSTRACT (Maximum 200 words) To improve signal to noise ratio (SNR), it is typical to stack receiver functions calculated from events at similar distances and back azimuths. We have adapted the velocity spectrum stacking (VSS) technique from reflection seismology to stack data with different ray parameters and improve the SNR. The VSS technique exploits differences in the shapes of the moveout curves of converted phases and reverberations to separate phases and infer velocity structure. By applying conventional receiver function techniques to the IRIS/IDA seismographic station at Obninsk, Russia we infer a 2 km thick slow velocity surface layer and a 47 km depth to Moho with relatively uncomplicated crustal structure. By comparing VSS computed for OBN and Arti (ARU), Russia with PREM synthetics we have identified Ps phases from the 400 and 670 km discontinuities. We find mantle structure characterized by higher S velocities and deeper discontinuities than PREM. We find no evidence of a 210 km discontinuity beneath either station. VSS comparisons between OBN and ARU imply that the 670 km discontinuity is about 2 km shallower beneath ARU than OBN.				
14. SUBJECT TERMS Seismology, Russia, mantle structure, crustal structure			15. NUMBER OF PAGES 58	
			16. PRICE CODE	
17. SECURITY CLASSIFICATION OF REPORT Unclassified		18. SECURITY CLASSIFICATION OF THIS PAGE Unclassified	19. SECURITY CLASSIFICATION OF ABSTRACT Unclassified	20. LIMITATION OF ABSTRACT SAR

CONTENTS

1.	INTRODUCTION	1
2.	METHOD	2
3.	SYNTHETIC EXAMPLE	5
4.	EARTH FLATTENING TRANSFORMATION	8
5.	EFFECTS OF RAY PATHS ON VSS WHEN APPLIED TO UPPER MANTLE DISCONTINUITIES	10
6.	CRUSTAL STRUCTURE AT OBN	13
7.	UPPER MANTLE DISCONTINUITIES AT OBN	14
8.	UPPER MANTLE DISCONTINUITIES AT ARU	16
9.	CONCLUSIONS	18
	REFERENCES	19

DTIC QUALITY INSPECTED 3

Accession For	
NTIS GRA&I	<input checked="" type="checkbox"/>
DTIC TAB	<input type="checkbox"/>
Unannounced	<input type="checkbox"/>
Justification	
By _____	
Distribution/ _____	
Availability Codes	
Dist	Special
A-1	

ILLUSTRATIONS

Figure 1. Ray paths for the Ps phase relative to the P phase for a layer over a half space. T_P and T_S are the travel times of the P and S phases with the same ray parameter through the layer respectively. T_h is the travel time differential in the half space for the two rays assuming a planar wave front.

Figure 2. Seismic section of synthetic receiver functions computed for a range of ray parameter from 0.040 to 0.080 by raytracing through a model with a 40 km thick layer ($V_P=6.0$ km/s, $V_S=3.5$ km/s) over a half space ($V_P=8.0$ km/s, $V_S=4.6$ km/s).

Figure 3. Ray paths for the P2p1s phase relative to the P phase for a layer over a half space. T_P and T_S are the travel times of the P and S phases with same ray parameter through the layer respectively. T_h is the travel time differential in the half space for the two rays assuming a planar wave front.

Figure 4. Velocity spectrum stacks produced from the synthetic receiver functions depicted in Figure 2. Ps stacks are shown on the left and P2p1s stacks are on the right.

Figure 5. Stacks of the synthetic receiver functions depicted in Figure 2. On top is a straight stack with no time correction applied. The bottom three receiver function stacks are computed after applying the appropriate normal moveout correction for Ps, P2p1s, and P1p2s respectively (from top to bottom).

Figure 6. Moveout curves at various depths from 25 km to 700 km for the Ps phase computed for the PREM velocity structure. The solid lines are moveout curves

computed for a single layer with equivalent average slowness as PREM to the respective depths. The dashed line is the moveout computed for a curved ray path by ray tracing through PREM. The depths associated with each curve are printed on the left.

Figure 7. Moveout curves at various depths from 25 km to 700 km for the P2p1s phase computed for the PREM velocity structure. The solid lines are moveout curves computed for a single layer with equivalent average slowness as PREM to the respective depths. The dashed line is the moveout computed for a curved ray path by ray tracing through PREM. The depths associated with each curve are printed on the left.

Figure 8. A representative display of the 80 low pass filtered (corner frequency of 0.3 Hz) PREM synthetic receiver functions used to compute the VSS in later figures. The moveout curve associated with Moho and upper mantle discontinuities are labeled. The dashed lines are the true moveout curves produced by raytracing through PREM. The solid lines are the moveout curves computed by replacing PREM with a layer over a that would result in a vertical travel time equivalent to that of PREM.

Figure 9. Spherical earth velocity spectrum stacks computed using the PREM synthetics depicted in Figure 8. The plot to the left was computed for Ps phases while the one on the right was computed using the P2p1s moveout curve.

Figure 10. The VSSc produced from the PREM synthetics depicted in Figure 8. The VSSc on the top was computed using PREM P and S velocities as the reference model. The reference model used to produce the two VSSc on the bottom used P velocities from PREM (left) and K8 (right) and a value of 1.825 for R_v .

Figure 11. Velocity ratio spectrum stacks (R_VSS) computed using PREM (left) and K8 (right) reference models for the synthetic receiver functions generated for the PREM model.

Figure 12. A representative sampling of the 113 low pass filtered individual receiver functions computed for OBN. The only clear arrivals without stacking are the Ps conversion from the Moho at 5 seconds and, in a few receiver functions the P2p1s and P1p2s from the Moho at 20 and 23 seconds respectively.

Figure 13. Synthetic (solid line) and observed (dashed line) stacked receiver functions computed for the IRIS/IDA Seismographic station at Obninsk. The synthetics pertain to the crustal structure models depicted on the left of the respective receiver functions. The low pass filtered response (stack of the receiver functions given in Figure 12) is given in the top frame; the broad band results are in the bottom frame.

Figure 14. Velocity spectrum stacks produced from the OBN receiver functions shown on Figure 8. The plot on the left was computed for Ps phases while the one on the right was computed using the P2p1s moveout curve.

Figure 15. The VSSc produced from 113 OBN receiver functions using PREM as the reference model.

Figure 16. Velocity ratio spectrum stack (R_VSS) from the OBN receiver functions computed using PREM as the reference model.

Figure 17. VSS_c computed from OBN receiver functions similar to that shown in Figure 15, except in this case, the VSS_c was computed using a value of 1.78 for R_v .

Figure 18. Velocity spectrum stacks produced from receiver functions computed from seismograms recorded at ARU. The plot on the left was computed for P_s phases while the one on the right was computed using the $P2p1s$ moveout curve.

Figure 19. Velocity ratio spectrum stack (R_vSS) from the ARU receiver functions computed using PREM as the reference model.

Figure 20. VSS_c computed from ARU receiver functions similar to that shown in Figure 19, except in this case, the VSS_c was computed using a value of 1.78 for R_v .

SUMMARY

In order to improve the signal to noise ratio of receiver function data, it is typical to stack receiver functions calculated from events at similar distances and back azimuths. We have adapted the velocity spectrum stacking (VSS) technique, used extensively in reflection seismology, to the receiver function method in order to stack data with different ray parameters, thereby improving further the signal to noise ratio. Perhaps more importantly, by producing the velocity spectrum stacks we take advantage of the differences in the shapes of the moveout curves of converted phases and reverberations to identify and separate the various phases and to infer velocity structure. Through conventional receiver function techniques we have modeled the crustal structure beneath the Russian IRIS/IDA seismographic station at Obninsk, Russia (OBN). This model includes a 2 km thick low velocity surface layer and 47 km depth to Moho with relatively uncomplicated crustal structure. By computing velocity spectrum stacks from the observed seismograms at OBN and Arti (ARU), Russia, and comparing them with those produced from PREM synthetics we have identified Ps phases from the 400 and 670 km discontinuities. We find that these phases can be interpreted satisfactorily in terms of a mantle structure characterized by higher upper mantle S velocities, and possibly deeper discontinuities than in PREM and in these data we find no evidence of a 200 km discontinuity beneath either of these stations. By comparison of VSS between OBN and ARU we suspect that the 670 km discontinuity is about 2 km shallower beneath ARU than OBN.

1. INTRODUCTION

A commonly used technique to estimate crust and upper mantle structure from a single three-component seismographic station is to compute and interpret "receiver functions" (e.g., Langston 1989, 1981, 1979, 1977; Owens, et al. 1984, 1987, 1988; Owens and Crosson 1988), wherein the horizontal components are deconvolved by the vertical component to produce a trace consisting primarily of Ps conversions and converted S-wave reverberations. The technique has been successfully extended to arrays of broadband portable stations by Owens et al. (1988a,b). To improve the signal to noise ratio, receiver functions can be binned by ray parameter and back azimuth and stacked (Owens et al. 1983; Owens 1984). In areas with flat geological structure the receiver functions show little or no azimuthal dependence and can be stacked at common ray parameter for all azimuths. However, if we wish to stack traces with different ray parameters, we must first correct for the differences in relative arrival times.

The "velocity spectrum stack" (VSS) is a useful tool for stacking reflection data within a range of ray parameters in multichannel studies (e.g. Yilmaz 1987). The functional dependence of arrival times on ray parameter p , relative to a reference phase with ray parameter p_0 is called the "moveout". The "normal moveout correction" (NMO) then refers to the time adjustment necessary to correct the arrival time to what would have been observed from a vertically incident ray, irrespective of amplitude, assuming a given velocity structure. The "velocity spectrum stack" (VSS) is a contour map of amplitudes across constant velocity stacks (produced by stacking the observed records after NMO assuming a uniform velocity) in the velocity-time plane (e.g. Sheriff 1982). A phase present in the receiver functions is thus enhanced in the VSS if the appropriate NMO correction is made. The enhancement will be most effective for a value of velocity matching the "true" mean velocity sampled by the phase. It is most

appropriate at this point to think of the velocity structure as a function of time since arrival time is observed whereas depth will be computed after the velocity structure is determined (Yilmaz 1987). Because of differences in the shapes of their moveout curves, separate stacks must be produced for each of the prominent phases present in the receiver functions. Therefore, the velocity spectrum stacks can be used to distinguish between phases as well as to infer velocity structure.

The examples in the following sections, describing the production of VSS, use radial components of the receiver functions. Since the production of the VSS depends only on travel time, the tangential component VSS can be produced using the same procedure, however for truly one-dimensional structure there will be no energy on the tangential components. Since the emphasis of this paper is the technique most of the explanations will use synthetic data. We will, however, discuss VSS produced from three component broad band seismograms recorded at Russia IRIS/IDA stations at Obninsk (OBN) and Arti (ARU).

2. METHOD

Figure 1 illustrates the geometry of the most significant type of phase observed in receiver function studies — the P to S conversion (Ps) generated when the wave crosses an interface — for a layer over a half space. We assume a planar incoming wave front (a typical assumption in receiver function studies) in deriving the following equations. The time delay for the Ps arrival relative to that of the P arrival $\Delta T_{Ps}(p)$ is given by:

$$\Delta T_{Ps}(p) = T_S + T_h - T_P \quad (1)$$

$$\Delta T_{Ps}(z,p,V_S,V_P) = z \left(\sqrt{V_S^2 - p^2} - \sqrt{V_P^2 - p^2} \right) \quad (2)$$

In the above equations: T_S , T_h and T_P are travel times along the paths labeled in Figure 1; V_S and V_P are the average S and P velocities in the layer, respectively; p is the ray parameter; and z is the depth to the interface. In terms of the vertical travel time of Ps relative to P (ΔT_{Ps0}) through the layer and the velocity ratio $R_V = V_P / V_S$, we have:

$$\Delta T_{Ps}(\Delta T_{Ps0}, p, V_S, R_V) = \frac{R_V \Delta T_{Ps0}}{R_V - 1} \left(\sqrt{1 - p^2 V_S^2} - \sqrt{R_V^{-2} - p^2 V_S^2} \right) \quad (3)$$

Note that this equation depends only on ΔT_{Ps0} , p , V_S and an assumed value for R_V (e.g. $R_V = \sqrt{3}$ for a Poisson solid).

Figure 2 depicts a set of synthetic receiver functions generated for a layer ($V_P = 6.0$ km/s, $V_S = 3.5$ km/s) over a half space ($V_P = 8.0$ km/s, $V_S = 4.6$ km/s, and $z = 40$ km) for a range of ray parameters. We see that the Ps phase is delayed with increasing ray parameter relative to the initial P-wave, illustrating the Ps moveout. All phases (reverberations) following Ps are advanced in arrival time relative to the P phase with increasing ray parameter. The next prominent phase after the Ps arrival is composed of the sum of all reverberations in which there are two P legs and one S leg. Figure 3 depicts the travel path of the Ppps phase in which the first two branches are P waves and the final branch is an S. For near vertical incidence the reverberations ending in an S leg will contribute much more energy to the horizontal components than those ending in a P (i.e. P spp, and P psp). For convenience of notation we will adopt a naming convention for the sum of these reverberations as Pn pms, in which n is the number of p legs and m is the number of s legs (if n or m is zero it is omitted). The phase described will be referred to as P2p1s. The next phase on Figure 2, P1p2s, composed of the sum of reverberations with two S legs and one P, has two

contributions with final S legs (the Psp and Pps) and a less significant Pssp contribution.

We take advantage of this difference in the shape of the moveout curve to distinguish reverberations from the Ps phase. Equation 4 gives the time delay (ΔT_{P2p1s}) for the P2p1s phase relative to the P arrival for a layer over a half space:

$$\Delta T_{P2p1s}(\Delta T_{P2p1s0}, \rho, V_S, R_V) = \frac{R_V \Delta T_{P2p1s0}}{R_V + 1} (\sqrt{1 - p^2 V_S^2} + \sqrt{R_V^{-2} - p^2 V_S^2}) \quad (4)$$

In like fashion, we can derive moveout equations for the P3p, P1p2s and P3s phases. However P3p and P3s have small amplitudes (even after stacking a very large number of events) so are usually of little significance in interpretations. P1p2s, on the other hand, has reversed polarity and is easily distinguishable from Ps and P2p1s, so we found it a useful phase in the interpretation of receiver structure at OBN. The moveout for this phase is given by:

$$\Delta T_{P1p2s}(\Delta T_{P1p2s0}, \rho, V_S, R_V) = \frac{2 R_V \Delta T_{P1p2s0}}{R_V + 1} \sqrt{1 - p^2 V_S^2} \quad (5)$$

Constant velocity stacks are produced by averaging along the moveout curve the amplitudes of N receiver functions with various ray parameters.

$$S(\Delta T_{\Phi 0}, V_S) = \frac{1}{N} \sum_{i=1}^N f_i(\Delta T_{\Phi}(\Delta T_{\Phi 0}, \rho_i, V_S, R_V)) \quad (6)$$

In this equation, Φ is the type of phase (e.g. Ps or P2p1s); $S(\Delta T_{\Phi 0}, V_S)$ is the averaged amplitude at a given zero offset time and S-wave velocity;

$f_i\{\Delta T_\Phi(\Delta T_{\Phi 0}, \rho_i, V_s, R_V)\}$ is the amplitude of the i^{th} trace at the computed moveout time, $\Delta T_\Phi(\Delta T_{\Phi 0}, \rho_i, V_s, R_V)$, for a given wave type (Φ). If the moveout time falls between two samples we linearly interpolate a value for $f_i\{\Delta T_\Phi(\Delta T_{\Phi 0}, \rho_i, V_s, R_V)\}$. After producing constant velocity stacks for the range of all reasonable velocities, we contour the amplitudes in the velocity-time plane to produce the VSS. The Ps conversion or P2p1s reverberation on their respective velocity spectrum stacks will appear as positive ridges (negative for a velocity inversion) elongated parallel to the velocity axis. The velocity structure beneath a station can then be inferred by selecting the time and velocity of the highest amplitude on each ridge.

An alternative to the summation of receiver function amplitudes along the moveout curve to generate a VSS is the normalized summation of the zero lag crosscorrelation of all the receiver functions in a small window (usually the wavelength of the expected arrival) centered about the moveout curve (Yilmaz, 1987). We have found that the advantages gained by this approach are usually cosmetic and occasional instabilities arise when it is applied to noise free synthetics or data in which the moveout curves of the Ps phase and reverberations cross. Although in some cases it may be beneficial to produce VSS by crosscorrelation, we feel that this does not add substantially to the major points of this paper and refer the reader to discussions in reflection seismology texts (e.g. Yilmaz, 1987).

3. SYNTHETIC EXAMPLE

Figure 4 depicts VSS produced for the Ps and P2p1s phases using the synthetic receiver functions shown in Figure 2. Upon inspection of the Ps stack (left) we observe good time resolution for Ps near 5 seconds but poor velocity resolution. This phase also appears on the P2p1s stack (right), but the peak is not as sharp and does not have as large an amplitude as on the Ps stack. P2p1s (at 18 s) is only observed on the

P2p1s stack and has much better velocity resolution than Ps. It is not surprising that we are able to pick $V_S=3.5$ km/s (the velocity used to compute the synthetics in Figure 2) more accurately from the P2p1s stack, since Figure 2 shows twice as much moveout for P2p1s than for Ps. We can use this velocity together with the approximate 4.8 s arrival time on the Ps stack to compute the thickness of the layer. The arrival times on the VSS are for vertically incident rays ($p=0$), so equation (2) becomes:

$$z = T_{Ps} / \{1/V_S - 1/V_P\} \quad (7)$$

For this shallow structure, we assume a poisson solid ($R_V = \sqrt{3}$) and solving for z we confirm the 40 km depth to the interface.

Figure 5 depicts single stacks of the receiver functions shown in Figure 2. The top stack has no moveout applied - the next three are stacked using the respective Ps, P2p1s, and P1p2s moveout curves (from top to bottom). In each case the respective velocity depth (time) function was picked by observation of the stacking amplitudes on the corresponding VSS (Figure 4). The P, Ps, P2p1s, and P1p2s arrivals are at 5, 10, 23 and 28 seconds respectively. Figure 5 clearly illustrates the fact that the various arrivals are substantially enhanced when stacked along the appropriate moveout curve. An added bonus is the annihilation of the reverberations (P2p1s and P1p2s) on the Ps stack; conversely the Ps phase is greatly diminished on the two reverberation stacks. We conclude that by producing the stacks with normal moveout we may identify arrivals that would otherwise not be observed and, in the process, avoid mislabeling other phases.

Figures 6 and 7 depict the shapes of the Ps and P2p1s moveout curves computed for various depths using the PREM velocity model (Dziewonski and Anderson, 1981) over the range of ray parameters typical of teleseismic P-arrivals used in receiver function studies (0.04 to 0.08 s/km for epicentral distances of 30° to 90°). For each given depth, the solid curve was computed for a single layer with average slowness (P

and S) equivalent to that of PREM. The dashed lines are the moveout curves computed to include the additional time delay resulting from the curvature of the ray path through PREM, discussion of which we defer to a later section. At this time, we shall merely point out that the curvature of the ray paths affects significantly the shape of the moveout curves only for interface depths greater than about 200 km.

For an interface depth of 50 km, there are 0.75 s of moveout over the teleseismic range of ray parameter. There are about 2.5 s of moveout calculated over the same range of ray parameter for the P2p1s phase at 50 km depth. In Figure 4 we observed that for an even shallower depth (40 km), with less moveout, reasonable signals appeared on the VSS for both phases. For the Ps phase, there are 1.8 s of moveout at 100 km over the range of ray parameters, and as much as 16.1 s at 600 km. It is clear that with a finite number of traces to stack, VSS produced for the Ps phase will be much more useful in the interpretation of upper mantle structure than of crustal structure. On the other hand, about 1.25 seconds of moveout is expected for the P2p1s over the given range of ray parameter at 25 km depth. Because of the greater amount of moveout calculated for this phase, its VSS may prove to be more valuable in the interpretation of shallow structure. On the other hand, the longer ray paths of the reverberations (as opposed to the direct Ps) make such phases more sensitive to heterogeneities in the near surface structure. As a result interpretation of these phases may often be more difficult (e.g., Owens et al. 1984).

It is clear from Figure 6 that to produce reliable VSS for Ps phases from shallow layers (100 km or less), data from the full range of ray parameters are necessary. For the Ps phases from deeper interfaces and the P2p1s phase at all depths, it appears that there is sufficient moveout along the curves to produce VSS from data with poorer distribution in slowness. In cases where there is not enough distribution of data to use the VSS method to estimate velocity structure, coherence between individual receiver

functions may still be improved, prior to stacking, by making a moveout correction (not necessarily normal moveout) using velocities from a regional model.

4. EARTH FLATTENING TRANSFORMATION

Traditionally, receiver functions are used to model crustal structure and it is adequate to assume a flat earth. In the case of upper mantle discontinuities, the curvature of the earth becomes a significant factor. Because all the moveout equations derived above were based on a flat-layered earth, we may use a classical earth flattening transformation (EFT, Biswas and Knopoff 1970; Aki and Richards, 1980) to map a flat earth structure into the spherical earth structure that will yield the equivalent seismograms. The transformation is not exact for P-SV waveforms, but it is exact for their travel times (Chapman 1973). Because the purpose of VSS is to sum the amplitudes of the receiver functions along the moveout curves in order to find the velocity and time delay for which the pulse of any given shape stacks most coherently, travel time preserving transformations will not reduce significantly the effectiveness of the VSS method.

The earth flattening transformation is applied to each grid cell of the VSS in order to convert the flat earth velocities (V_f) to spherical earth velocities (V_{sph}) according to:

$$V_f = V_{sph} (r/r_e) , \quad (8)$$

where r_e is the radius of the earth. Here, r is the radius corresponding to the grid cell and is related to the flat earth depth (z) by:

$$r = r_e e^{z/r_e} , \quad (9)$$

where z , for each grid cell of the time versus velocity VSS, is determined by equation (7) for Ps velocity spectrum stacks. For the P2p1s phase z is determined by:

$$z = T_{Ps} / (1/V_S + 1/V_P) \quad (10)$$

By performing this transformation on a flat earth VSS (VSS_f) generated similarly to that of Figure 4 we obtain the spherical earth VSS (VSS_{sph}).

Figure 8 shows synthetic receiver responses of a planar P wave front passing through PREM over the range of ray parameter from 0.04 to 0.08 s/km. Each of these receiver functions was low pass filtered with a corner frequency of 0.3 Hz in order to match the observations at OBN discussed below. Figure 9 depicts the VSS_{sph} computed for these synthetics. We used a uniform R_V of 1.825 in computing the VSS_{sph} which is the appropriate average value for PREM to a depth of 670 km. The effect of this approximation—as opposed to using a depth-dependent ratio—will be the same on VSS_{sph} computed for synthetics and for those computed for observed data. Letting this ratio vary with depth would add another free parameter and unnecessarily complicate the discussion. The shallower arrivals (for which a lower value of R_V is appropriate) will stack at a slightly lower-than-expected velocity as a result of this approximation. The contour intervals for Figure 9 were chosen to emphasize the upper mantle discontinuities, so that crustal phases arriving in the first 25 seconds of the plot are saturated. The Ps conversions from the 400 and 670 km discontinuities appear at about 41 seconds and 63 seconds respectively on the Ps velocity spectrum (left). Because the Ps phase from the 200 km discontinuity is on the trailing edge of the Moho reverberations at 20 seconds there is no distinct arrival for it on the VSS; however the corresponding P2p1s phase appears strongly at 76 seconds on the P2p1s VSS_{sph} .

5. EFFECTS OF RAY PATHS ON VSS WHEN APPLIED TO UPPER MANTLE DISCONTINUITIES

In the previous section, we outlined the correction necessary to modify the VSS technique for application to deep structure. In this section we outline the procedures to correct for errors introduced resulting from the following "ray path" assumptions: 1) typically in VSS studies the effect of curvature of ray path is ignored; 2) in both receiver function and VSS studies a planar incoming wave front is assumed.

In the process of mapping the VSS_f into the VSS_{sph} we computed the radius for every grid cell on the VSS, so that we can plot the result as a velocity spectrum stack in the spherical-earth-depth versus velocity domain (VSS_z). However, returning to Figures 6 and 7, we observe that the "true moveout curves" produced by ray tracing through PREM exhibit a greater amount of moveout than those computed by replacing the PREM structure above the interface with a single layer of equal average vertical slowness. Because the amount of moveout is directly proportional to the increase in velocity, it is clear that computing moveout using the single layer assumption outlined above will result in a high estimate of velocity when applied to data from a layered structure. We notice in Figure 6 and 7 that the "true moveout curves" and the single layer moveout curves merge to the same zero offset time delay. As a result the time delays observed on the VSS_{sph} (Figure 9) are true zero offset travel times but the velocities are overestimated, which would result in an overestimate of the depths to the upper mantle discontinuities. This should affect observed data and synthetics in the same way, so that the procedure should be adequate to compare synthetics and observed data; it will of course work well for shallow layers. To estimate more accurately the velocity structure directly from VSS, we have refined our method of producing VSS_z by applying normal moveout corrections computed for curved ray paths (VSS_c).

The curved ray path normal moveout correction can be computed by ray tracing through a reference model. Because we do not need the amplitude information provided by ray tracing, it is quicker to compute moveout corrections by integrating the relative time delay (equations 2 through 4) due to each infinitesimally thin layer (dz) to the given depth (z₁).

$$\Delta T_{Ps}(z,p,V_S,V_P) = \int_0^{z_1} \left(\sqrt{V_S^2(z) - p^2} - \sqrt{V_P^2(z) - p^2} \right) dz \quad (11)$$

Equation (11) is used to compute the ΔT_{Φ} values required by equation (6) to produce "reference velocity model stacks" (RVMS) in the same manner that constant velocity stacks were produced in previous sections. By multiplying all velocities of the reference model by a constant fraction we compute a "fractional reference model". A VSS_c is then constructed by contouring RVMS produced for a range of different fractional reference models. The axes of the VSS_c are depth versus "fraction of reference model", therefore a phase identified on the VSS_c has a velocity which we describe as a certain fraction or percentage above or below the reference model.

The assumption of a planar wave front (i.e. that the P and the Ps phases have the same ray parameter) results in a slight error in the estimate of the shape of the moveout curve. This error behaves similarly to that described above for the curved ray path correction but results in only about a fifth as much error in the estimated velocity, and therefore would cause the estimate for the depth to the 670 km discontinuity to be shallow by about 5 km. For shallower layers, the error in depth estimates resulting from this assumption is negligible. To image accurately the 670 km discontinuity we must compute the moveout curves by ray tracing through reference models. In constructing the VSS_z by this technique we found that for certain fractional reference

models, the rays with large ray parameters would turn before reaching the surface. This information alone can be used to exclude certain fractional reference models from the set of possible solutions.

Figure 10 shows a P_s VSS_c for the same PREM synthetics used in computing Figure 9. The top VSS_c was computed using the PREM P and S velocities. The other two plots (bottom left and right, respectively) were computed using the PREM and the K8 P-velocity model for northwestern Eurasia (Given and Helmberger, 1980) and a value of $R_v = 1.825$. The fact that the leftmost and middle plots are virtually identical encourages us to believe that a model such as K8 would be a reasonable reference model provided that a reasonable value for R_v is used. The peaks associated with each arrival on the two PREM reference model VSS_c (left and center) line up along the value of 1.0 on the horizontal axis and appear at the expected 670 km depth. However this phase appears at about a fractional velocity model value of 0.99 and at a slightly greater depth on the K8 VSS_c . The average PREM velocity computed to this depth is about .985 that of K8, which is within the peak observed in K8 reference model VSS_c of Figure 10. This small difference in velocity results in the slight discrepancy in depth when applied to the large time delays associated with upper mantle discontinuities.

By following the steps outlined above to generate the VSS_c except holding the model constant and varying the velocity ratio (R_v), we can produce a spectrum of stacked receiver functions (R_vSS) which will be most coherent at the proper value of R_v . Figure 11 depicts the R_vSS computed from the above PREM synthetics using PREM (left) and K8 (right) as reference models. For this synthetic example, we find indeed that for both reference models the expected value of $R_v = 1.82$ to 1.825 produces the greatest amplitude on the R_vSS .

6. CRUSTAL STRUCTURE AT OBN

We computed Velocity Spectrum Stacks for data recorded at the Russian station at Obninsk (OBN). We use conventional receiver response interpretation to constrain the crustal structure and use the VSS method in the following section to look at upper mantle discontinuities.

Receiver functions for the IRIS/IDA station at OBN were computed using data collected in 1989-90 (Gurrola, et al., 1990a,b). The station is equipped with a broadband three-component system with response nominally flat with respect to velocity from approximately 3 mHz to 5 Hz. We used teleseismic P and PP phases which, due to the uneven distribution of source regions during the one year period covered by the data, primarily sample the northeast and southeast quadrants. We found it useful to high-pass filter the seismograms in order to counter the effects of occasional nonlinear noise problems at frequencies lower than 20 mHz.

The broadband OBN receiver functions are dominated by reverberations within a shallow surface layer. In order to identify phases from deeper layers, we have reduced the contribution of the near surface layer by low-pass filtering these data with a phaseless Gaussian filter (with a half power width of 0.6 Hz, Figure 12). The velocity structure was determined using the smooth inversion of Ammon (Ammon, et al., 1990), which employs the reflection matrix method (Kennett, 1983; and Randall, 1989). The simplest model that we could construct which satisfies both the broadband and the high frequency data includes a low velocity surface layer of no more than 2.5 km thickness and a rather smoothly increasing velocity gradient to the 47 km deep Moho as shown on Figure 13 (Gurrola et al. 1990a).

7. UPPER MANTLE DISCONTINUITIES AT OBN

VSS_{sph} produced from OBN receiver functions (Figure 14) exhibit clear arrivals from the upper mantle discontinuities. The P_s VSS_{sph} is depicted on the left and the $P2p1s$ VSS_{sph} is on the right of the figure. We observe P_s and $P2p1s$ phases from the Moho at about 5 and 20 seconds respectively. The contour interval was chosen to illustrate best the upper mantle arrivals not observable on the individual receiver functions, so that Moho arrivals are not well defined on these plots. We used the same value for R_V (1.825) as used in the PREM VSS discussed above.

The observed P_s phase from the 400 km discontinuity (at 41 seconds on the VSS_{sph} of Figure 14) is larger in amplitude than the P_s phase from the 670 km discontinuity. This is the opposite of our observations of the PREM synthetics in which the P_s from the 400 km discontinuity was 2/3 the amplitude of that of the 670 km discontinuity (Figure 9). This result is consistent with the larger velocity contrast for the 400 km discontinuity suggested by the K8 continental model of Given and Helmberger (1980). Because K8 is only specified in terms of P velocities, synthetics produced for it will be heavily dependent upon the necessary assumption of S velocity and density, therefore we did not produce a synthetic VSS_{sph} for this model. The P_s arrival from the 670 km discontinuity is similar in amplitude on both the OBN stacks and the PREM synthetics, which implies a similar velocity contrast. This phase appears to arrive slightly earlier in time and at a higher velocity in the OBN VSS_{sph} than on the PREM VSS_{sph} . The time delay between the 400 and 670 km discontinuities is smaller than observed in PREM, which is consistent with a conclusion reached by Vinnik, based on independent analysis of OBN data (L. Vinnik, 1990, personal comm.). From Figure 15 (the VSS_c computed for the P_s moveout curve) we observe that the expected P_s phase from the 670 km discontinuity actually stacks best as a phase from a depth of 665 km with a velocity of about 1.04 times that calculated from PREM. From this we

may infer that this discontinuity is either 5 km shallower beneath OBN than predicted by PREM or that the value of R_V beneath OBN is lower than in PREM. Figure 16 depicts R_V SS produced from the OBN receiver functions using PREM as the reference model. Because the peak on this R_V SS is broad, it would be impossible to pick an exact value of R_V for which the receiver functions stack best. It is clear, however, that the data stacks best for values of R_V less than the average 1.825 value computed from PREM. Using the value of R_V at the center of the peak in this figure (about 1.78) with PREM P-velocities we produced the VSS_c shown in Figure 17. From this figure, we infer a depth to the 670 km discontinuity of about 675 km with a fractional velocity multiplier of about 1.01. In light of the fact that the P-velocities inferred from Figure 17 are greater than those of the reference models, the simplest physical interpretation of a low V_p/V_s ratio is in terms of higher S velocities due to a more rigid upper mantle than implied by PREM. This is consistent with the fact that PREM, being a global model, is biased toward oceanic structure: one may expect that beneath the Russian Platform the mantle is older and cooler, resulting in greater rigidity. Shearer and Masters, (1991) give evidence (related to the topography of the 670 km discontinuity beneath the subduction zones along the northeastern rim of the Pacific Ocean) that a decrease in the temperature of the upper mantle will result in a greater depth to the 670 km discontinuity and elevated seismic velocities. We favor the interpretation that the depth to this discontinuity beneath OBN is greater than 670 km and that the V_p/V_s ratio is low because this explanation requires a smaller velocity perturbation with respect to both K8 and PREM and it is consistent with the R_V value determined by R_V SS. However it is clear from VSS_c (Figures 15 and 17) that for any reasonable value of R_V the average velocity in the upper mantle is higher than that computed for either of the reference models.

We do not observe a 200 km discontinuity beneath OBN. For the PREM model, the P_s phase from the 200 km discontinuity arrives just after the P_{2p1s} from the Moho

resulting in a broader peak at 20 seconds on the synthetic VSS_{sph} (Figure 9) than on the observed. The strong P2p1s arrival from the 200 km discontinuity observed at 75 seconds on the PREM VSS_{sph} is not apparent in observed VSS_{sph} (Figure 14). These observations lead us to conclude that there is no 200 km discontinuity beneath OBN, or at least that it is not as pronounced as in PREM.

8. UPPER MANTLE DISCONTINUITIES AT ARU

Our discussion of the upper mantle structure observed in VSS produced for Arti, Russia (ARU) will draw heavily on comparisons with the observations for OBN. The receiver functions computed for ARU exhibited a surface layer response, but not as overwhelming as that observed in receiver functions produced for OBN. For the sake of comparison of VSS computed for these two stations, the receiver functions computed for ARU were low-pass filtered with the same gaussian filter used for OBN data.

The VSS_{sph} to the left on Figure 18 was computed using the moveout equation for the Ps phase; the one to the right was computed using the P2p1s moveout equation. On the Ps VSS_{sph} , the observe Ps phases from the 400 km discontinuity (at about 41 s) is slightly larger in amplitude than the Ps phase from the 670 km discontinuity (at about 61 s), which is similar to the amplitude relationship observed in the VSS_{sph} produced for OBN. This unusually large amplitude for the Ps phase from the 400 km discontinuity is not likely to be an artifact of our method because this phase is very weak to non-existent in VSS_{sph} produced for most other stations (Gurrola et al., 1992). The P2p1s phase from the 200 km discontinuity observed in the VSS_{sph} produced from the PREM synthetics is also absent in the P2p1s VSS_{sph} produced from the ARU receiver functions. This is a rather surprising result in view of the fact that Goldstein et al (1991) observed a phase that they interpret as a reflection from the 200

km discontinuity in recordings, from ARU, of nuclear blasts at the kazakh test site. Since the reflections observed by Goldstein et al. (1991) would be from hundreds of km away (at the midpoint between the Kazakh test site and ARU), it is possible that the 200 km discontinuity may become less pronounced closer to the station. Both OBN and ARU are located on the Russian Platform whereas Kazakh test site is over a thousand km from ARU on the other side of the Ural mountains. Perhaps this change in geological terrain is the reason the 200 km discontinuity is not observed in our VSS which sample the mantle within 150 km of the station. Alternatively, the 200 km discontinuity in this region may have a smaller velocity contrast than that of PREM, and the reflection method of Goldstein et al. (1991) may be more sensitive to this discontinuity than our method.

Figure 19 depicts a R_{VSS} computed for ARU. The peak in this figure is even more elongated than on the R_{VSS} computed for OBN, however the relationship of a lower than PREM (1.825) V_P/V_S ratio can be inferred for this station. For the sake of comparison with the results for OBN, we use the same V_P/V_S ratio to compute the $VSSc$ (Figure 20) for this station as employed in computing Figure 17. Comparing Figures 17 and 20, we observe that the peak for the P_s phase from the 670 km discontinuity is sharper for ARU than OBN. More importantly we observe that the peak as a whole on Figure 20 appears to shifted to the upper right corner of the plot relative to the peak on Figure 17 to a position about 2 km shallower in depth and no more than .01 higher in velocity ratio relative to PREM. We believe that this kind of comparison in relative depth and velocity between two stations is more reliable than trying to pick an absolute depth and velocity at a single station.

9. CONCLUSIONS

Through the use of velocity spectrum stacks we can stack receiver functions calculated from data with different ray parameters, and by doing so infer velocity structure beneath the seismographic station. This technique can be used to distinguish between a P_s phase and a $P2p1s$ reverberation based on differences in the shapes of their respective moveout curves. The method looks most promising for the interpretation of upper mantle structure, but when a full range of ray parameters is available, crustal structure might also be imaged with VSS. The shape of the moveout curve for a particular phase is dependent on the depth of the interface from which it originates and the velocity structure above the interface. In order to compute moveout for the curved ray path of P_s phases for upper mantle discontinuities, we trace rays through a reference model and infer a fractional difference between the reference model and the structure necessary to satisfy the data. It should be clear from the examples above that the depth of an interface from which the phase of interest originated is poorly constrained by the VSS method unless assumptions are made about the velocity structure or R_v . For OBN and ARU, we assumed that the PREM model P -velocities are reasonably close to the truth and inferred the value of R_v from a velocity ratio spectrum stack (R_vSS). Applying this R_v value to the PREM model produced a VSS_c from OBN receiver functions and yielded a 675 km depth for the "670 km discontinuity" with an average velocity about 1.01 times that of PREM. The inferred depth to the 670 km discontinuity beneath ARU is 2 km shallower than that of OBN with about the same velocity structure as OBN relative to PREM.

Through the analysis of VSS produced for data from OBN and ARU, we have identified upper mantle P_s conversions associated with the 400 km discontinuity that were not observable in the individual receiver functions. We have also obtained evidence that the 200 km discontinuity is not present or is weak beneath these

stations. By comparing the VSS produced from PREM synthetics with those produced from observed data we conclude that the greater velocity contrast across the 400 km discontinuity proposed in the K8 model (Given and Helmberger, 1980) for upper mantle structure beneath northwestern Eurasia is more appropriate for this station than that of PREM.

REFERENCES

- Aki, K, and P. G. Richards, 1980, Quantitative Seismology Theory and Method, *W. H. Freeman and Co.*, volume 1.
- Ammon, C. J., G. E. Randell, and G. Zandt, 1990, On the non-uniqueness of receiver functions inversions, *J. geophys. Res.*, **95**,1303-1318.
- Biswas, N. N. and L. Knopoff, 1970, Exact earth-flattening calculation for Love waves, *Bull. seism. Soc. Am.*, **60**, 1123-1137.
- Chapman, C. H., 1973, The Earth flattening transformation in body wave theory, *Geophys. J. R. astr. Soc.*, **35**, 55-70.
- Dziewonski, A.M. and D.L. Anderson 1981, Preliminary reference Earth model, *Physi. Earth and Planet. Int.*, **25**, 297-356.
- Given, J.W. and D.V. Helmberger, 1980, Upper mantle structure of northwestern Eurasia, *J. geophys. Res.*, **85**, 7183-7194.
- Goldstein, P., W.R. Walter, and G. Zandt, 1992, Upper mantle structure beneath central Eurasia using a source array of Nuclear explosions and wave form at regional distances, *J. of Geophys. Res.*, **97**, 14097-14113.
- Gurrola, H, J.B. Minster, T. Owens, and S. Madabhushi, 1992, Velocity spectrum stacks applied to receiver functions for the interpretation of upper mantle structure, *EOS*, **73**, abst. no. T21C-1.

- Gurrola, H, J.B. Minster, and T. Owens, 1990a, Receiver responses at IRIS/IDA stations in the USSR, 12th annual DARPA/GL Seismic Research Symposium, Geophysics Laboratory Hanscom AFB, Mass. GL-TR-90-0212, ADA226635.
- Gurrola, H, J.B. Minster, and T. Owens, 1990b, Receiver responses at IRIS/IDA stations in the USSR, *EOS*, 71, 1450.
- Langston, C.A., 1989, Scattering of teleseismic body waves under Pasadena, California, *J. geophys. Res.*, 94, 1935-1951.
- Langston, C. A., 1981, Evidence for the subducting lithosphere under southern Vancouver Island and western Oregon from teleseismic P wave conversions, *J. geophys. Res.*, 86, 3857-3866.
- Langston, C. A., 1979, Structure under Mount Rainier, Washington, inferred from teleseismic body waves, *J. geophys. Res.*, 84, 4749-4762.
- Langston, C. A., 1977, The effects of planar dipping structure on source and receiver responses for constant ray parameter, *Bull. seism. Soc. Am.*, 67, 1029-1050.
- Owens, T. J., R. S. Crosson, and M.A. Hendrickson, 1988, Constraints on the subduction geometry beneath western Washington from broadband teleseismic waveform modeling, *Bull. seism. Soc. Am.*, 78, 1319-1334.
- Owens, T. J., and R. S. Crosson, 1988, Shallow structure effects on broadband teleseismic P waveforms, *Bull. seism. Soc. Am.*, 78, 96-108.
- Owens, T. J., S. R. Taylor, and G. Zandt, 1987, Crustal structure at regional seismic test network stations determined from inversion of broadband teleseismic P waveforms, *Bull. seism. Soc. Am.*, 77, 631-662.
- Owens, T.J., G. Zandt, S.R. Taylor, 1984, Seismic evidence for an ancient rift beneath the Cumberland plateau, Tennessee: a detailed analysis of broadband teleseismic P waveforms, *J. geophys. Res.*, 89, 7783-7795.

- Owens, T. J., 1984, Determination of crustal and upper mantle structure from analysis of broadband teleseismic P-waveforms, *Ph.D. Dissertation*, University of Utah, Salt Lake City, Utah, 146 pp.
- Owens, T. J., S. R. Taylor, and G. Zandt, 1983, Isolation and enhancement of the response of local seismic structure from teleseismic structure from teleseismic P-waveforms, *internal report*, Lawrence Livermore Laboratory.
- Randall, G. E., 1989, Efficient calculation of differential seismograms for lithospheric receiver functions, *Geophys. J. R. astr. Soc.*, **99**, 469-481.
- Sheriff, R.E., 1982, Encyclopedic Dictionary of Exploration Geophysics, *Society of Exploration Geophysicists*, Tulsa, Ok.
- Vinnik, L.P., 1977, Detection of waves converted from P to SV in the mantle, *Physi. Earth and Planet. Int.*, **15**, 39-45.
- Yilmaz, O., 1987, Seismic Data Processing. *Society of Exploration Geophysicists, Investigations in Geophysics Volume 2.*

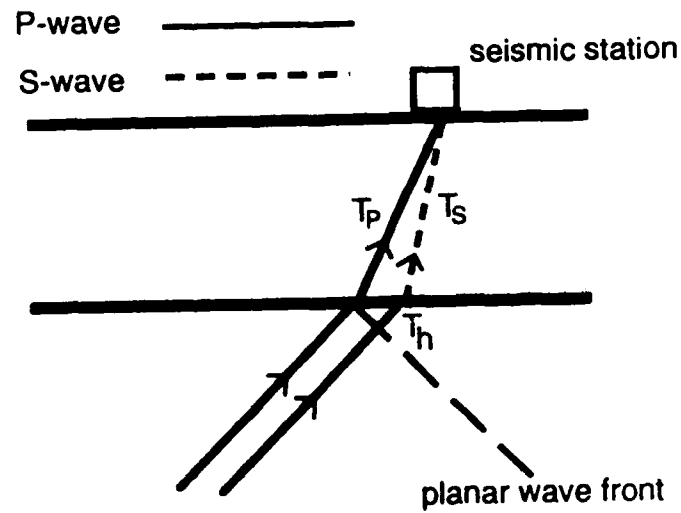


Figure 1. Ray paths for the Ps phase relative to the P phase for a layer over a half space. T_p and T_s are the travel times of the P and S phases with the same ray parameter through the layer respectively. T_h is the travel time differential in the half space for the two rays assuming a planar wave front.

Synthetic Receiver Functions

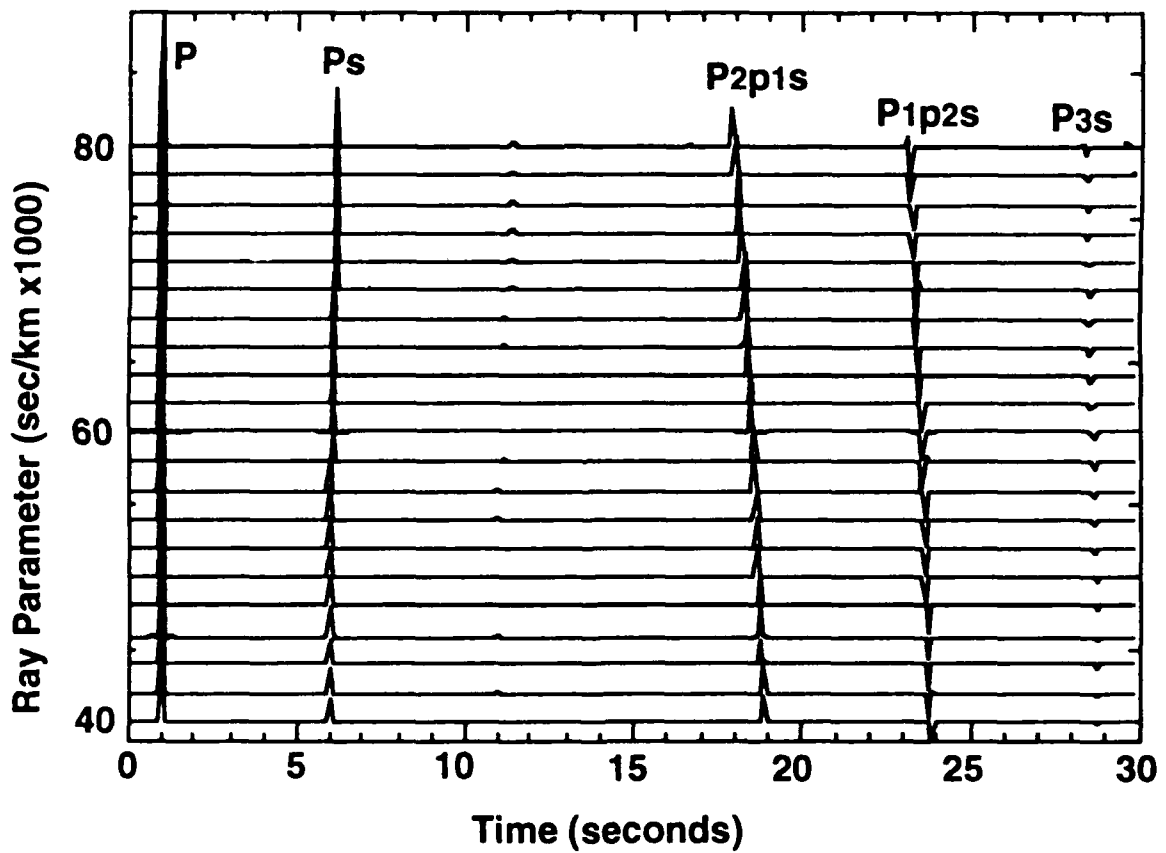


Figure 2. Seismic section of synthetic receiver functions computed for a range of ray parameter from 0.040 to 0.080 by raytracing through a model with a 40 km thick layer ($V_p=6.0$ km/s, $V_s=3.5$ km/s) over a half space ($V_p=8.0$ km/s, $V_s=4.6$ km/s).

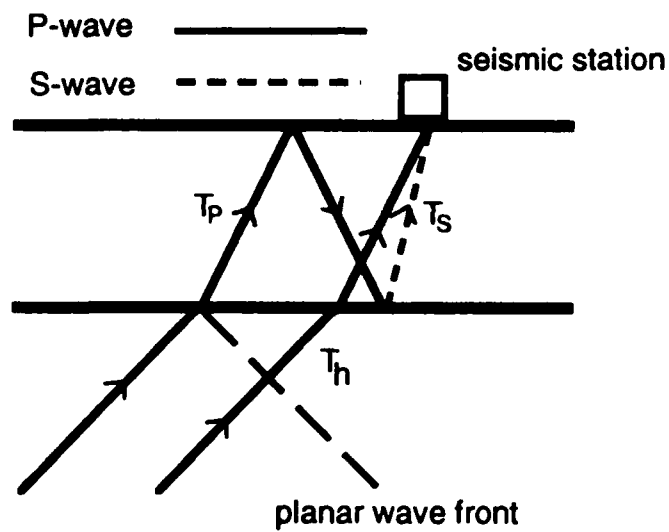


Figure 3. Ray paths for the P2p1s phase relative to the P phase for a layer over a half space. T_p and T_s are the travel times of the P and S phases with same ray parameter through the layer respectively. T_h is the travel time differential in the half space for the two rays assuming a planar wave front.

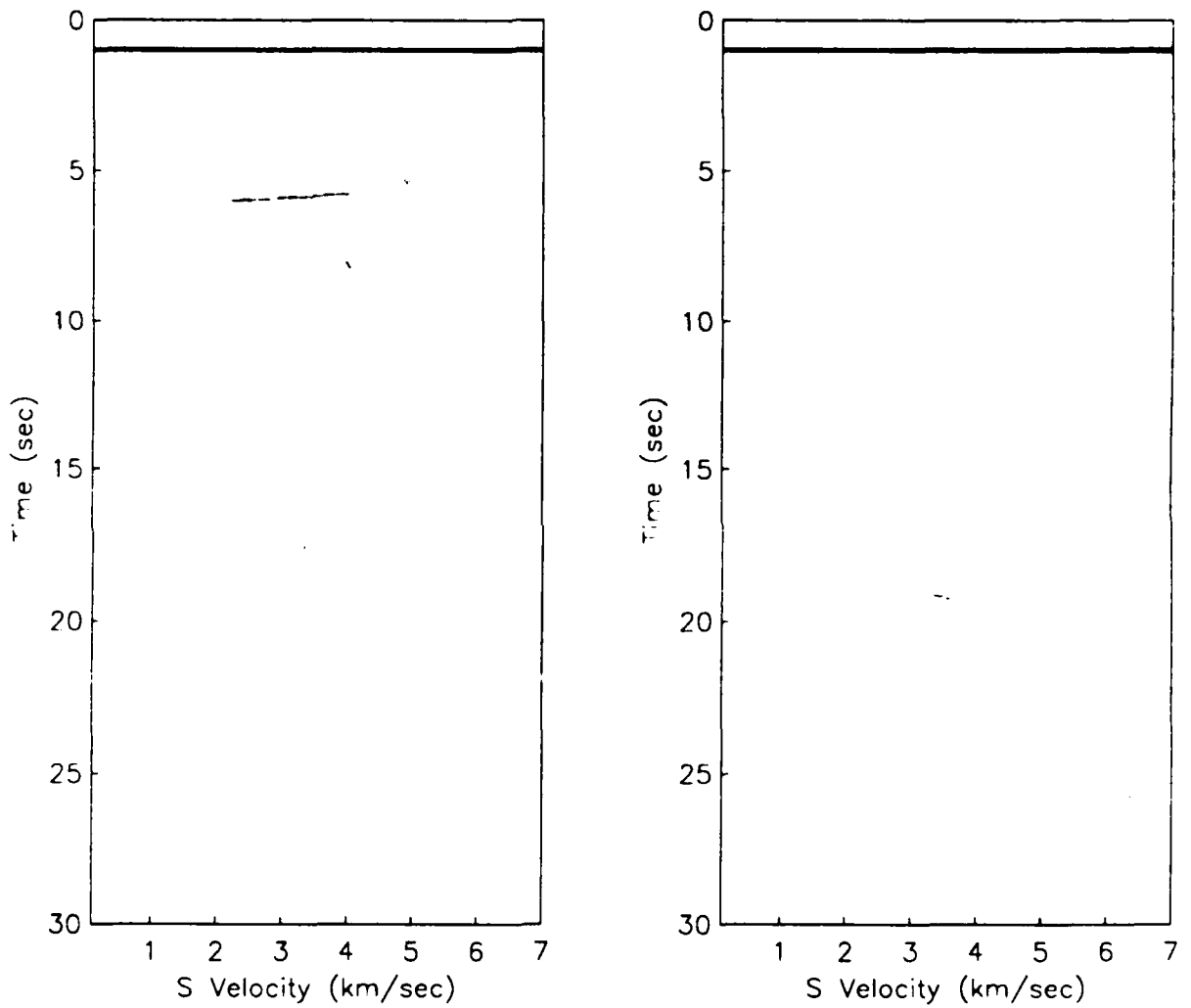


Figure 4. Velocity spectrum stacks produced from the synthetic receiver functions depicted in Figure 2. Ps stacks are shown on the left and P2p1s stacks are on the right.

Stacked Synthetic Receiver Functions

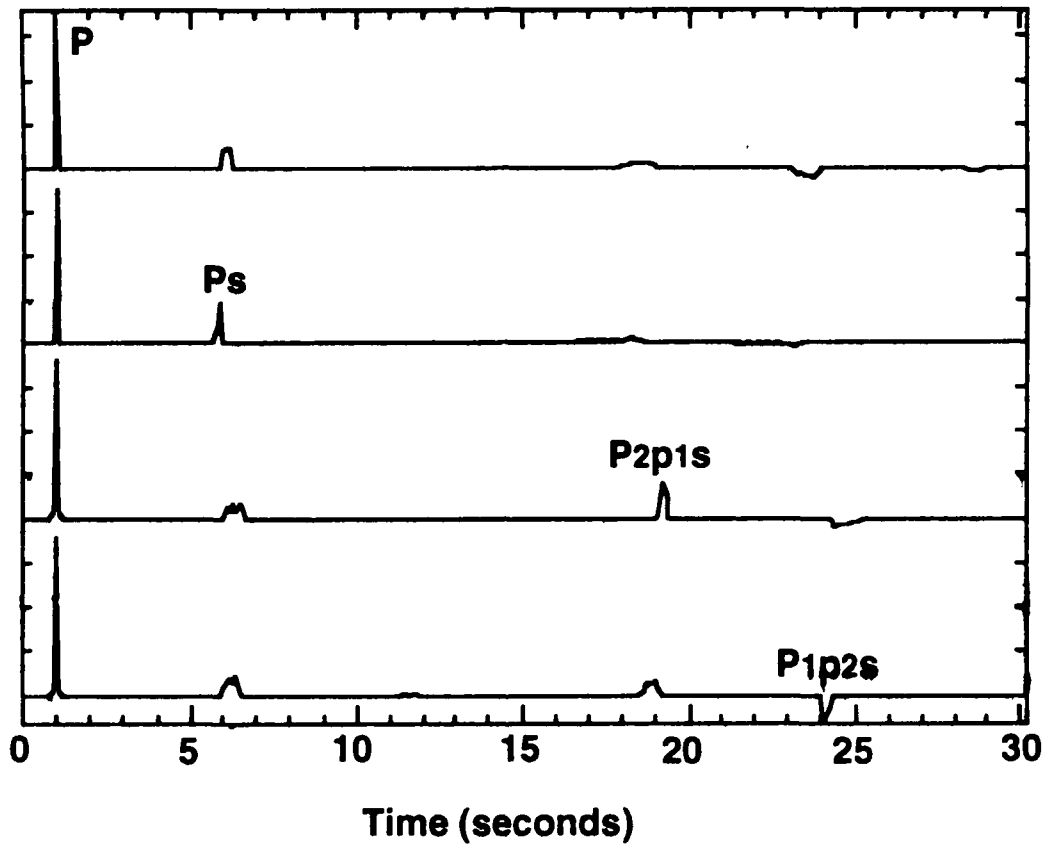


Figure 5. Stacks of the synthetic receiver functions depicted in Figure 2. On top is a straight stack with no time correction applied. The bottom three receiver function stacks are computed after applying the appropriate normal moveout correction for Ps, P2p1s, and P1p2s respectively (from top to bottom).

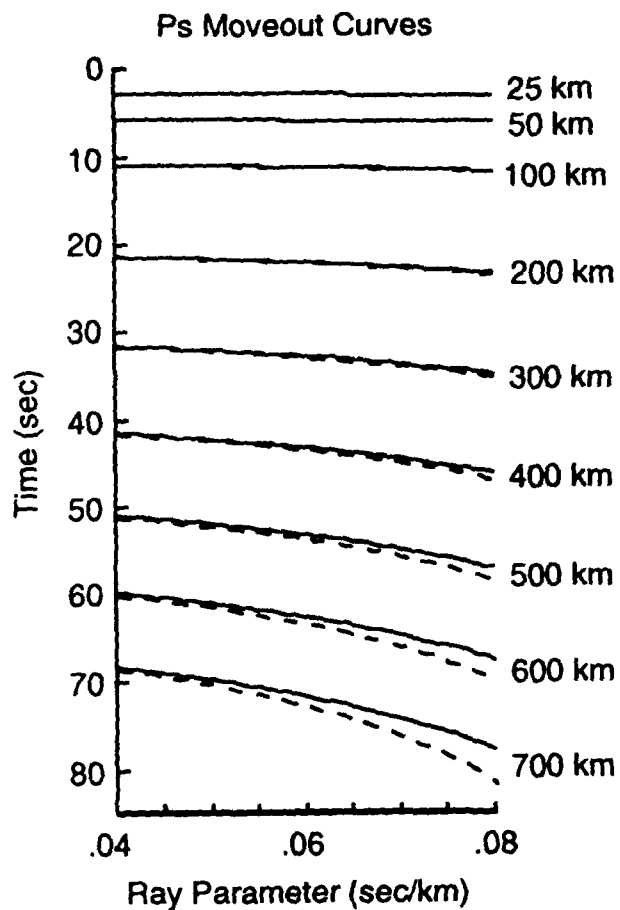


Figure 6. Moveout curves at various depths from 25 km to 700 km for the Ps phase computed for the PREM velocity structure. The solid lines are moveout curves computed for a single layer with equivalent average slowness as PREM to the respective depths. The dashed line is the moveout computed for a curved ray path by ray tracing through PREM. The depths associated with each curve are printed on the left.

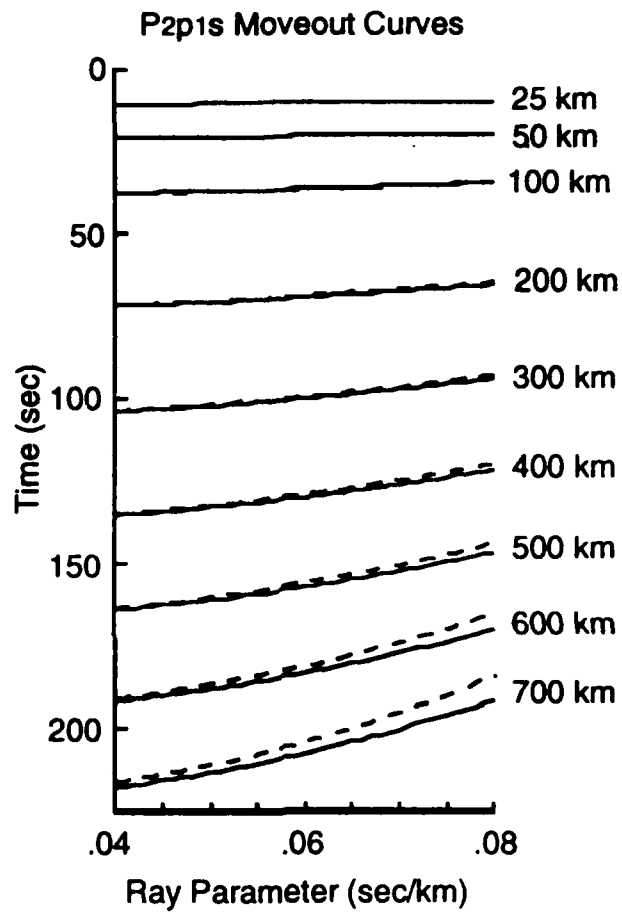


Figure 7. Moveout curves at various depths from 25 km to 700 km for the P2p1s phase computed for the PREM velocity structure. The solid lines are moveout curves computed for a single layer with equivalent average slowness as PREM to the respective depths. The dashed line is the moveout computed for a curved ray path by ray tracing through PREM. The depths associated with each curve are printed on the left.

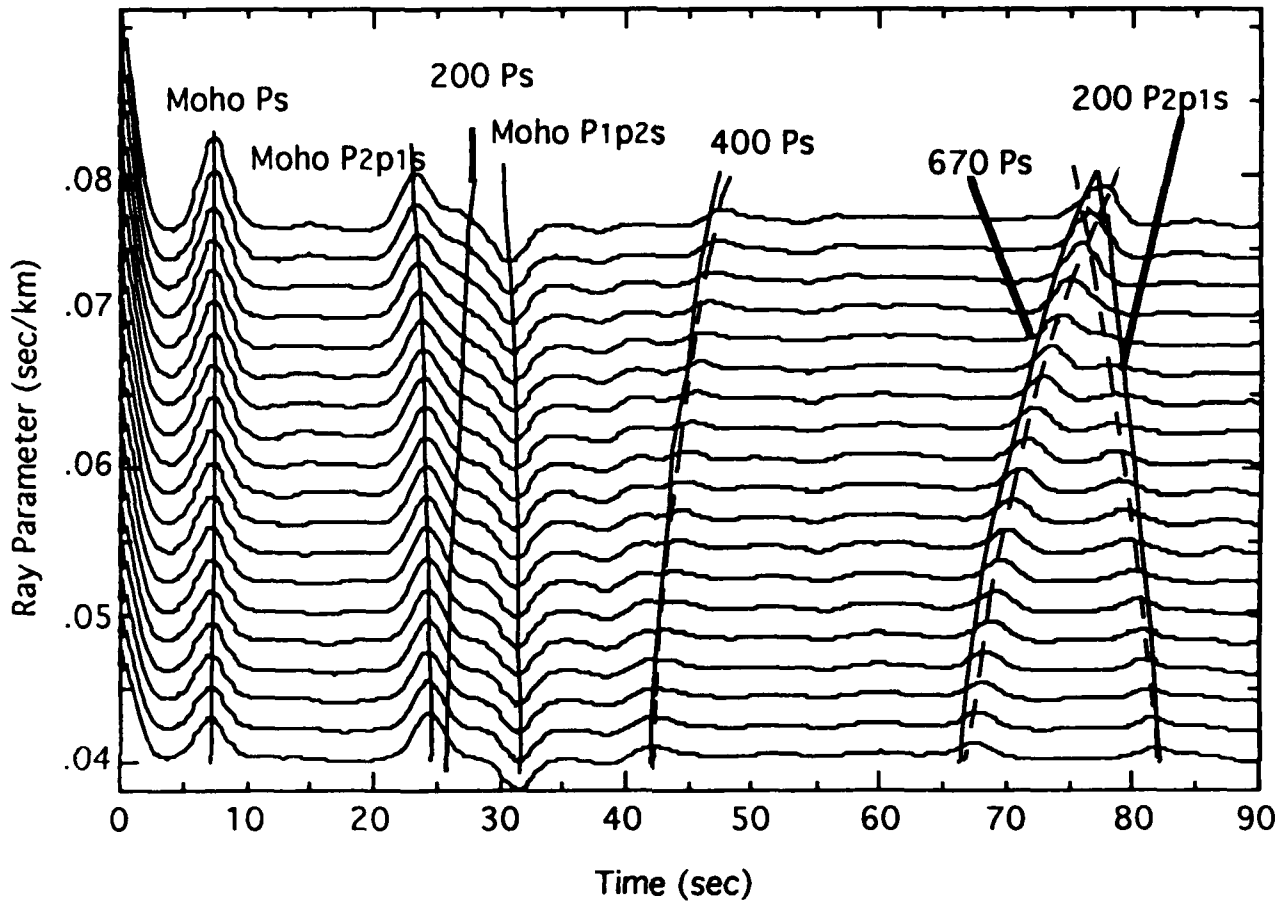


Figure 8. A representative display of the 80 low pass filtered (corner frequency of 0.3 Hz) PREM synthetic receiver functions used to compute the VSS in later figures. The moveout curve associated with Moho and upper mantle discontinuities are labeled. The dashed lines are the true moveout curves produced by raytracing through PREM. The solid lines are the moveout curves computed by replacing PREM with a layer over a that would result in a vertical travel time equivalent to that of PREM.

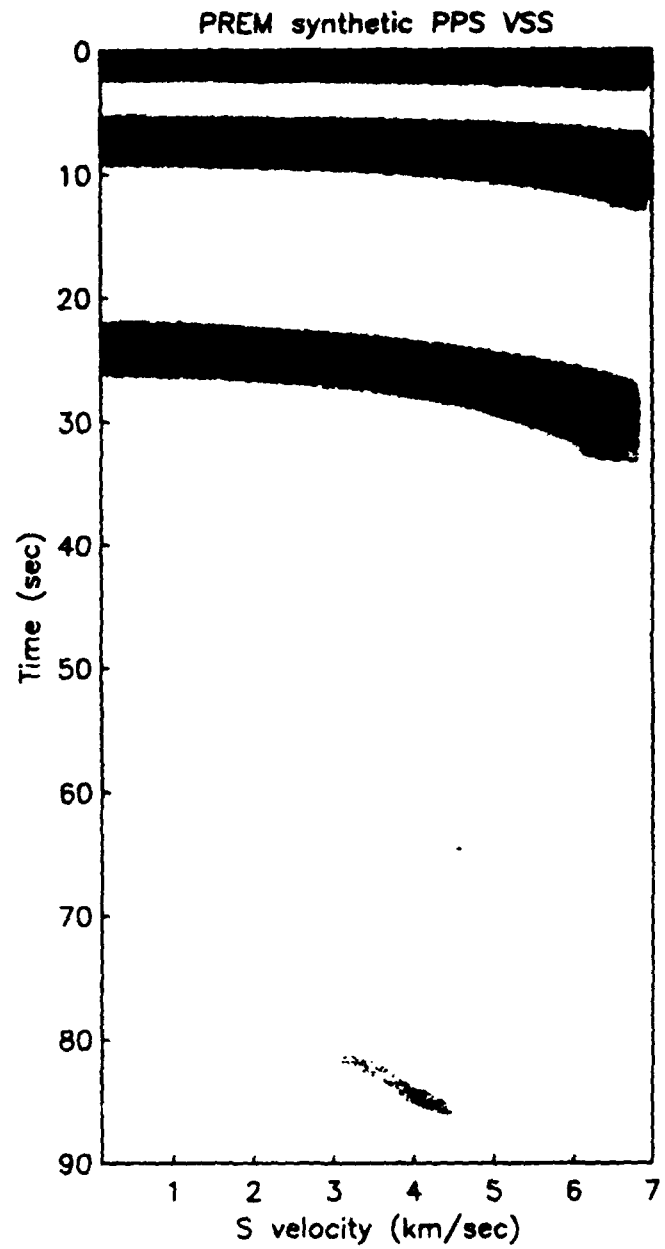
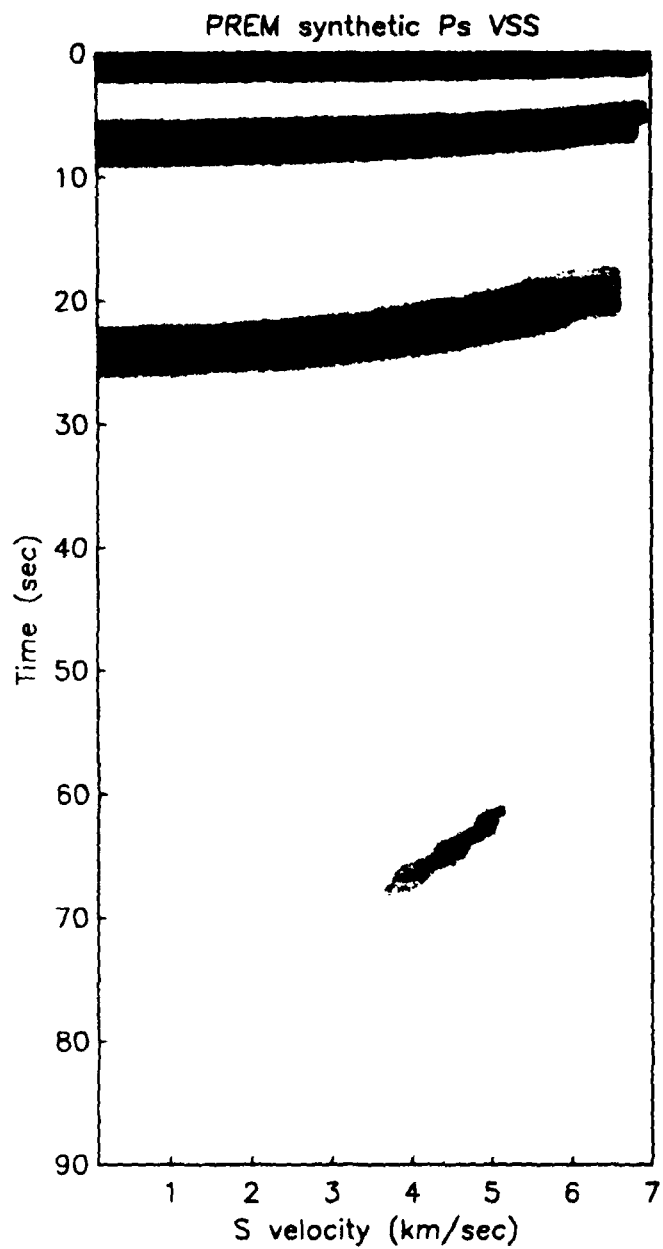


Figure 9. Spherical earth velocity spectrum stacks computed using the PREM synthetics depicted in Figure 8. The plot to the left was computed for Ps phases while the one on the right was computed using the P2p1s moveout curve.

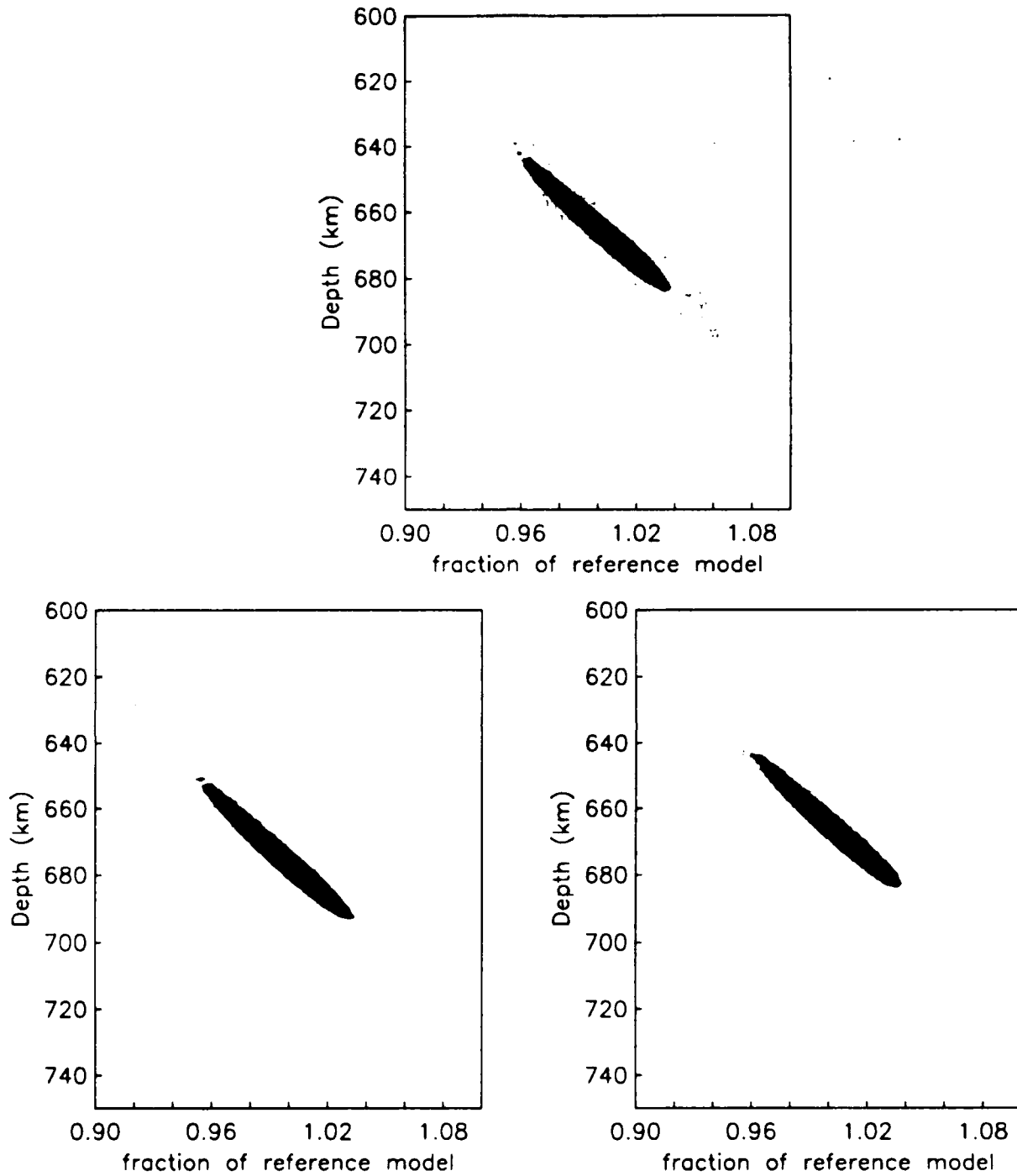


Figure 10. The VSSc produced from the PREM synthetics depicted in Figure 8. The VSSc on the top was computed using PREM P and S velocities as the reference model. The reference model used to produce the two VSSc on the bottom used P velocities from PREM (left) and K8 (right) and a value of 1.825 for Rv .

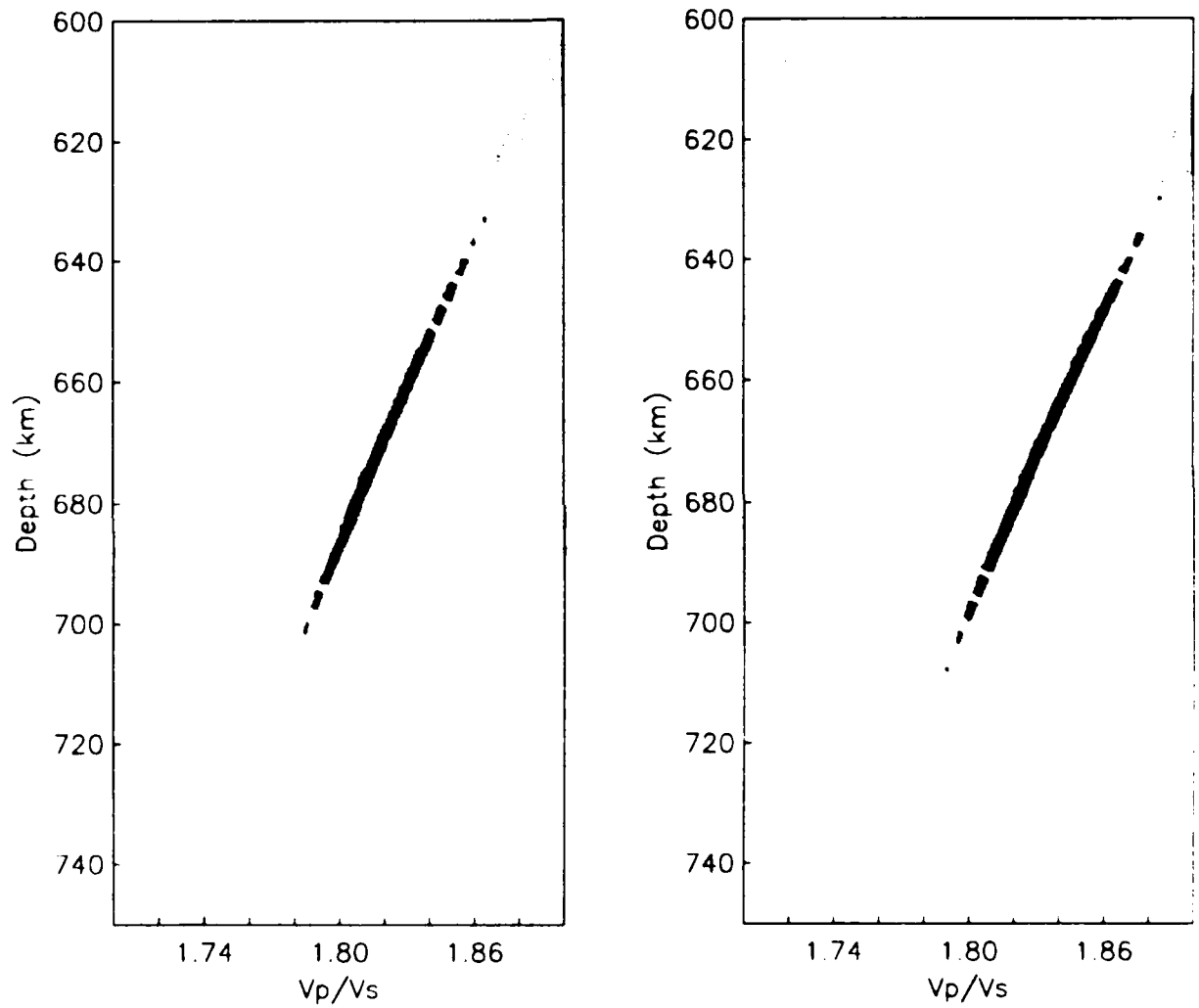


Figure 11. Velocity ratio spectrum stacks (R_{vSS}) computed using PREM (left) and K8 (right) reference models for the synthetic receiver functions generated for the PREM model.

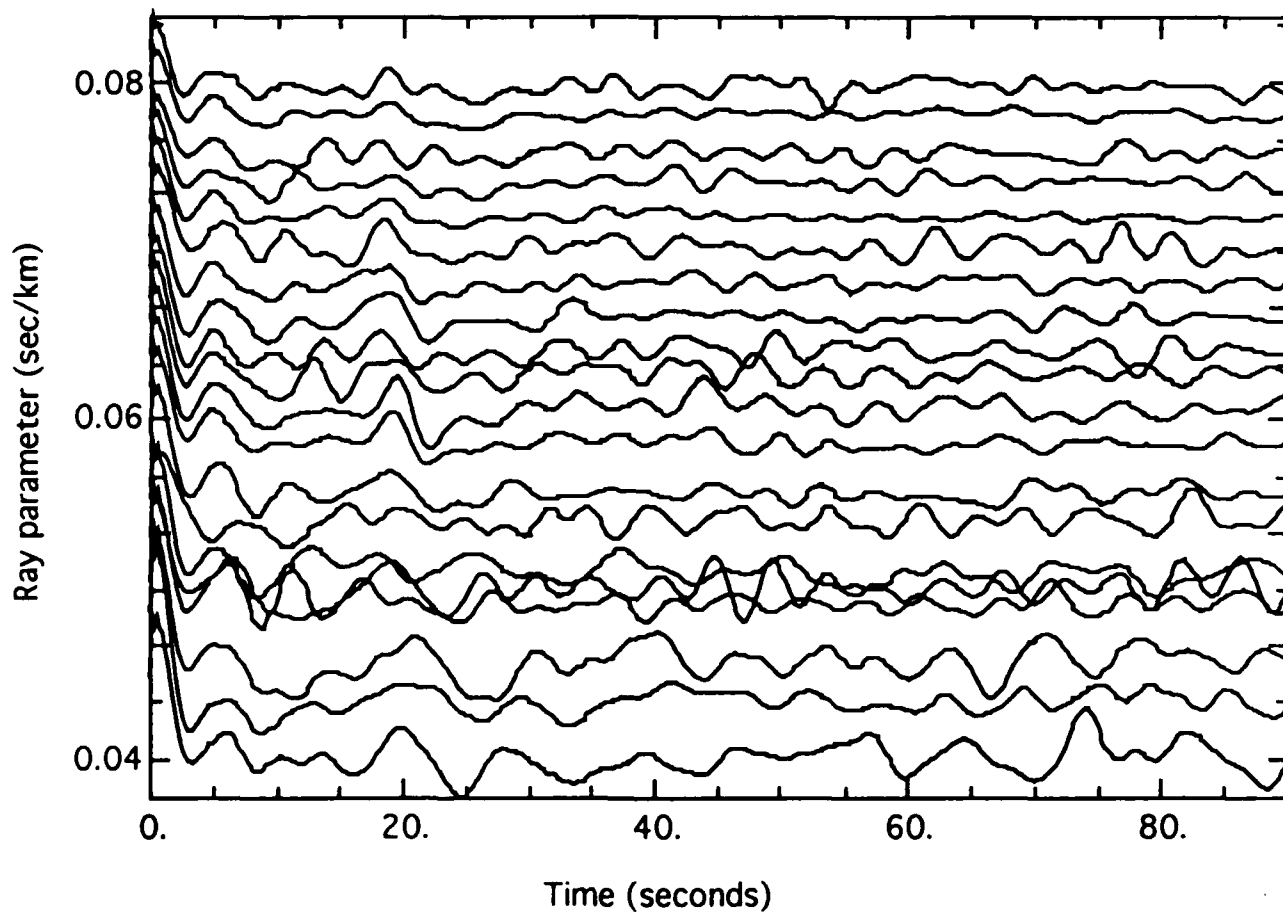


Figure 12. A representative sampling of the 113 low pass filtered individual receiver functions computed for OBN. The only clear arrivals without stacking are the P_s conversion from the Moho at 20 seconds and, in a few receiver functions the P₂p₁s and P₁p₂s from the Moho at 23 and 23 seconds respectively.

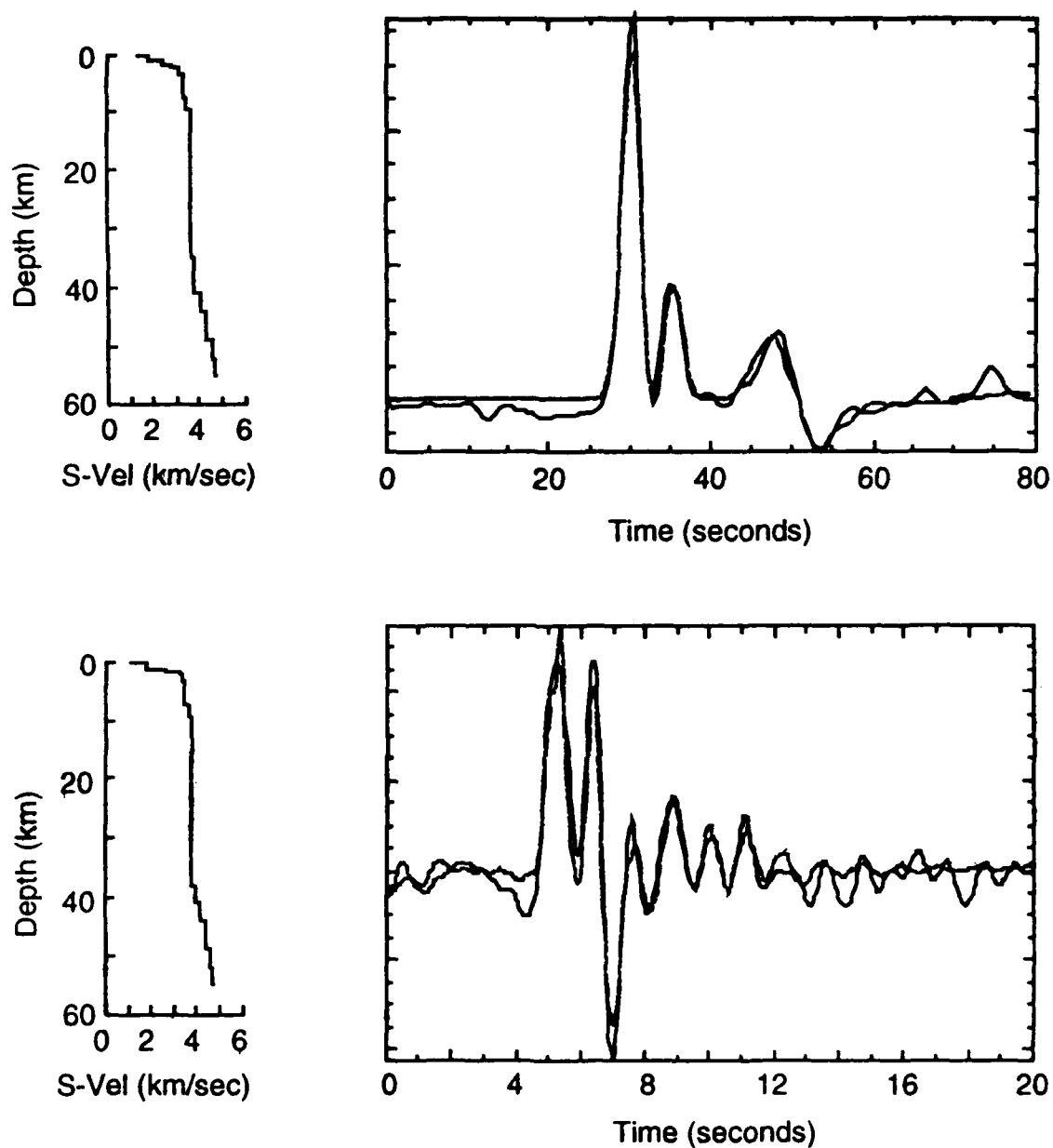
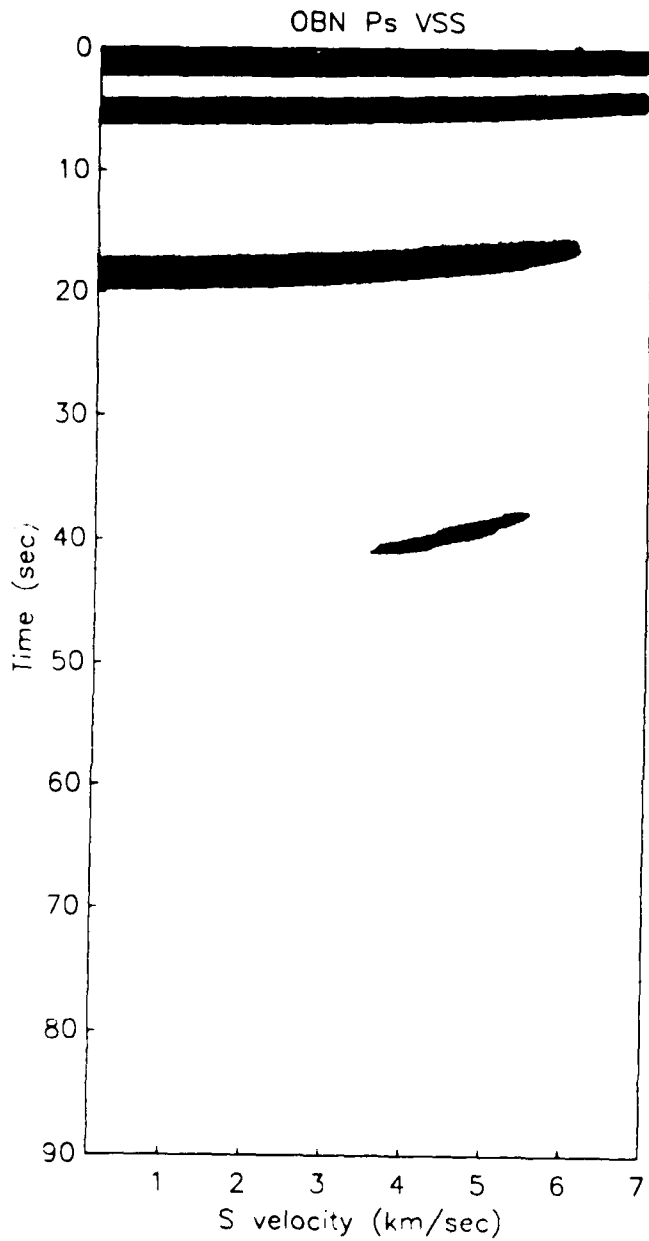


Figure 13. Synthetic (solid line) and observed (dashed line) stacked receiver functions computed for the IRIS/IDA Seismographic station at Obninsk. The synthetics pertain to the crustal structure models depicted on the left of the respective receiver functions. The low pass filtered response (stack of the receiver functions given in Figure 12) is given in the top frame; the broad band results are in the bottom frame.



113 events $\alpha = .6$ $v_p/v_s = 1.825$

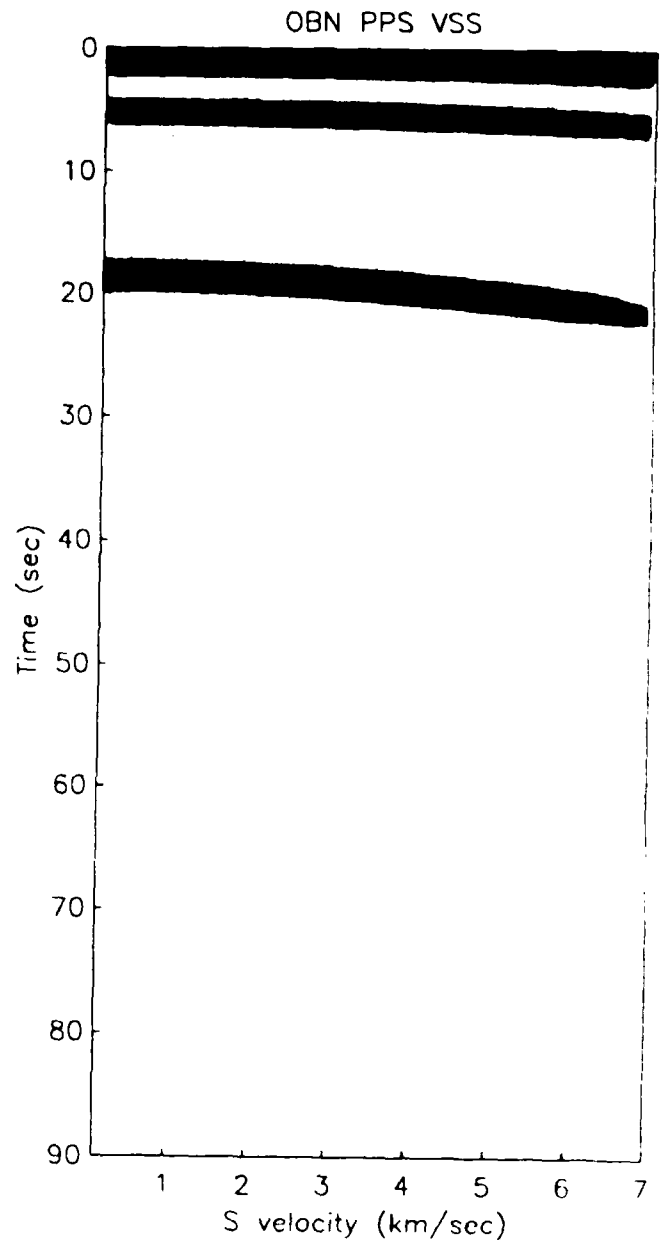


Figure 14. Velocity spectrum stacks produced from the OBN receiver functions shown on Figure 8. The plot on the left was computed for Ps phases while the one on the right was computed using the P2p1s moveout curve.

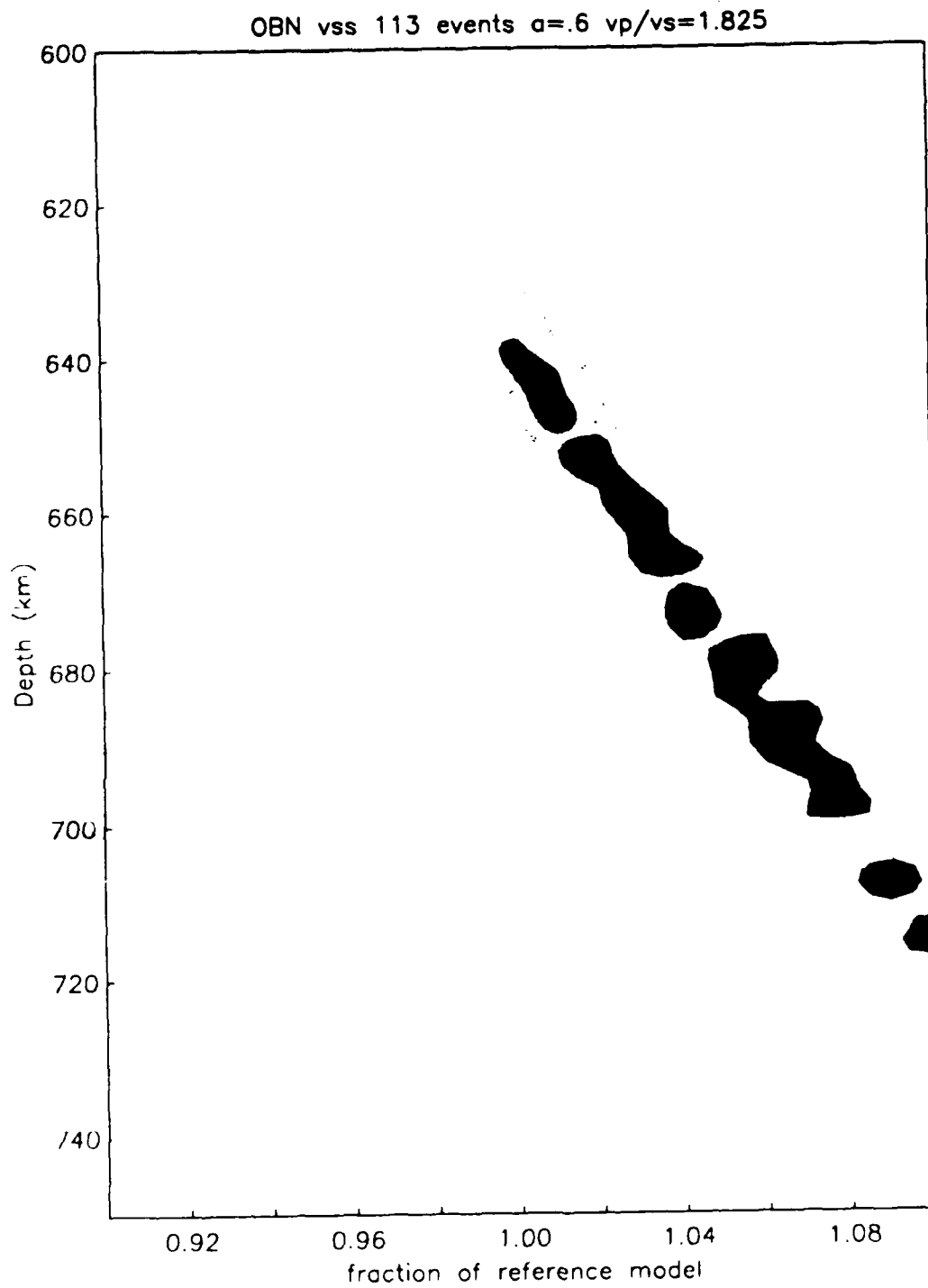


Figure 15. The VSSc produced from 113 OBN receiver functions using PREM as the reference model.

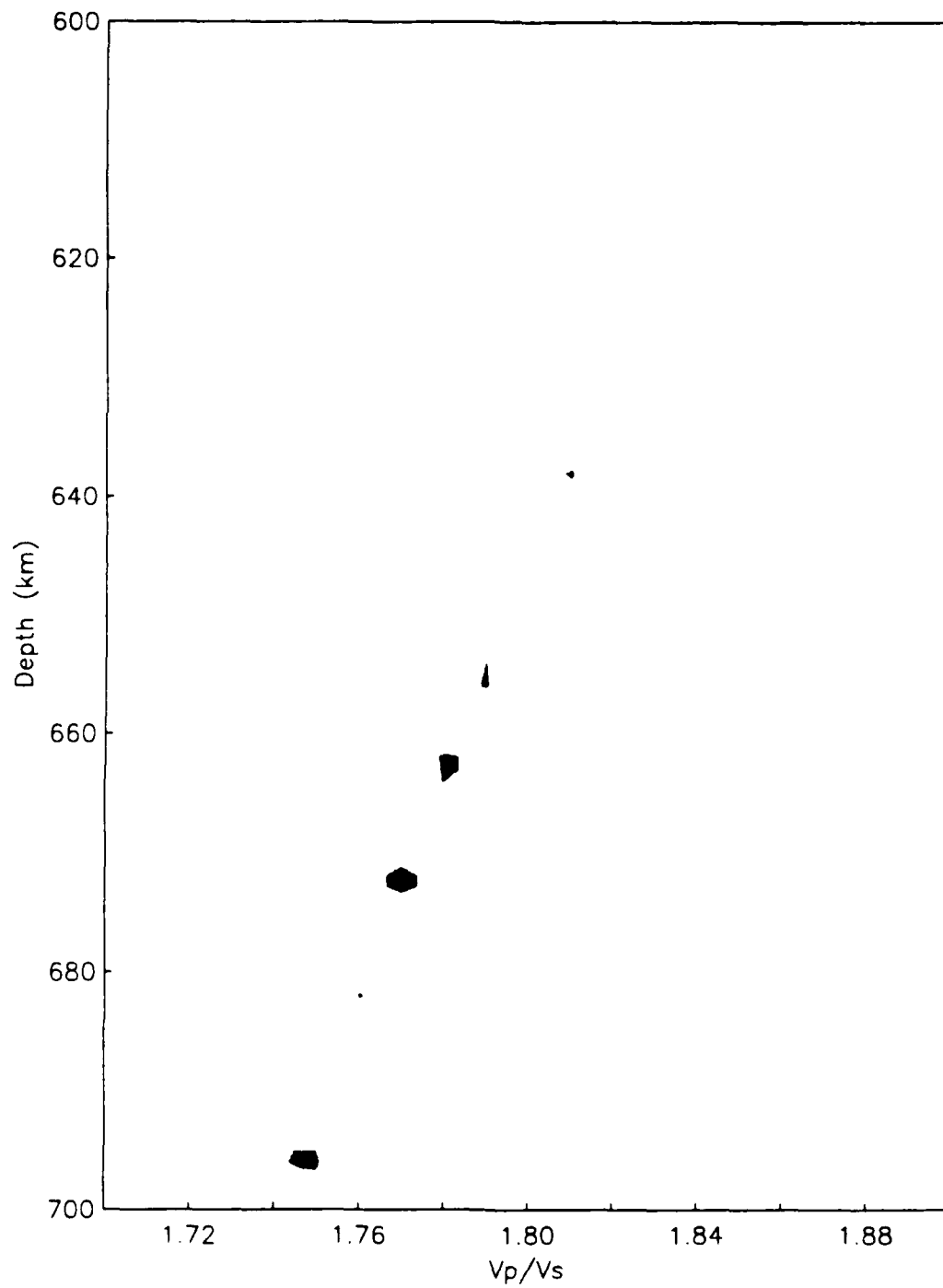


Figure 16. Velocity ratio spectrum stack (R_{VSS}) from the OBN receiver functions computed using PREM as the reference model.

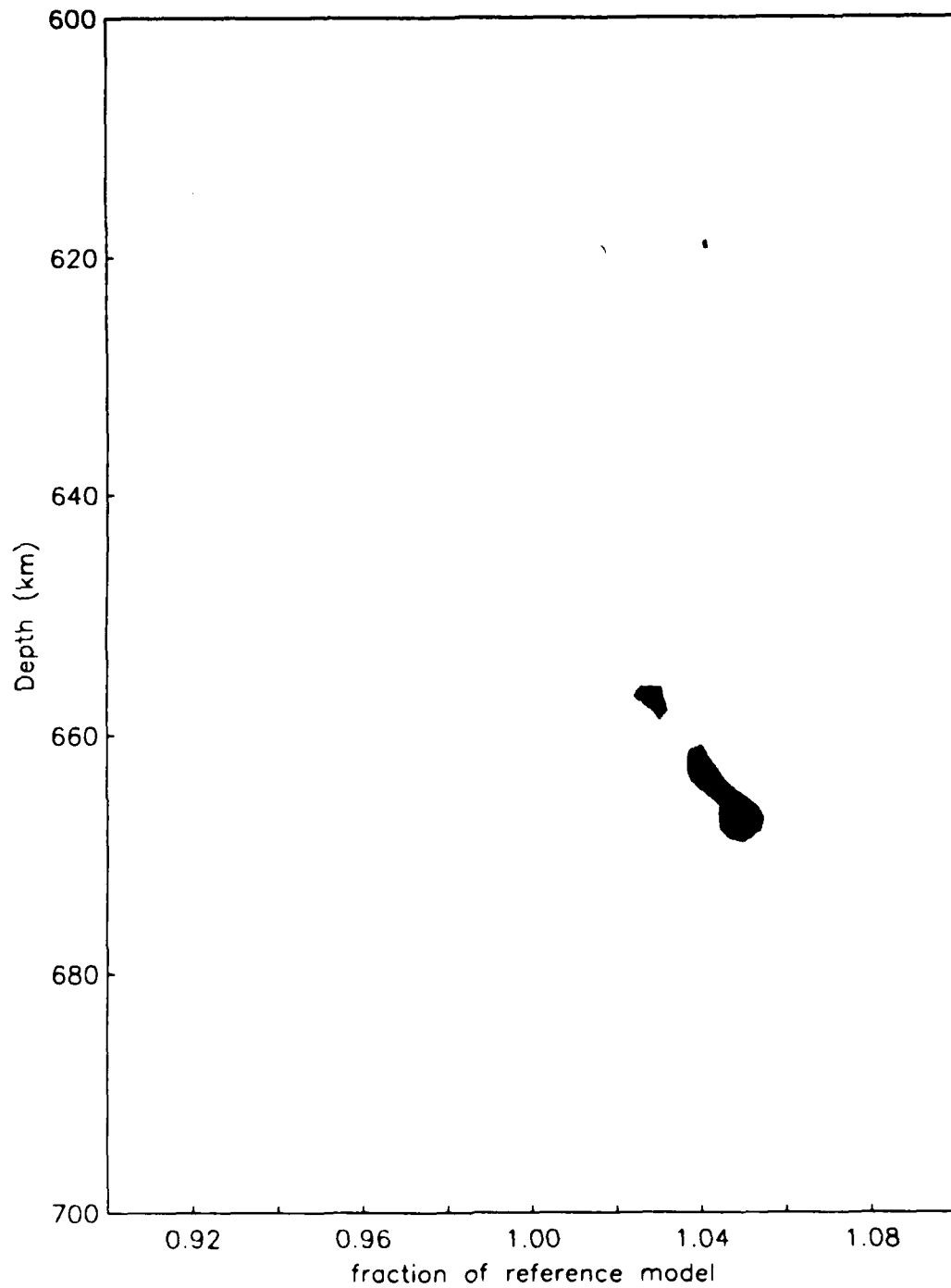
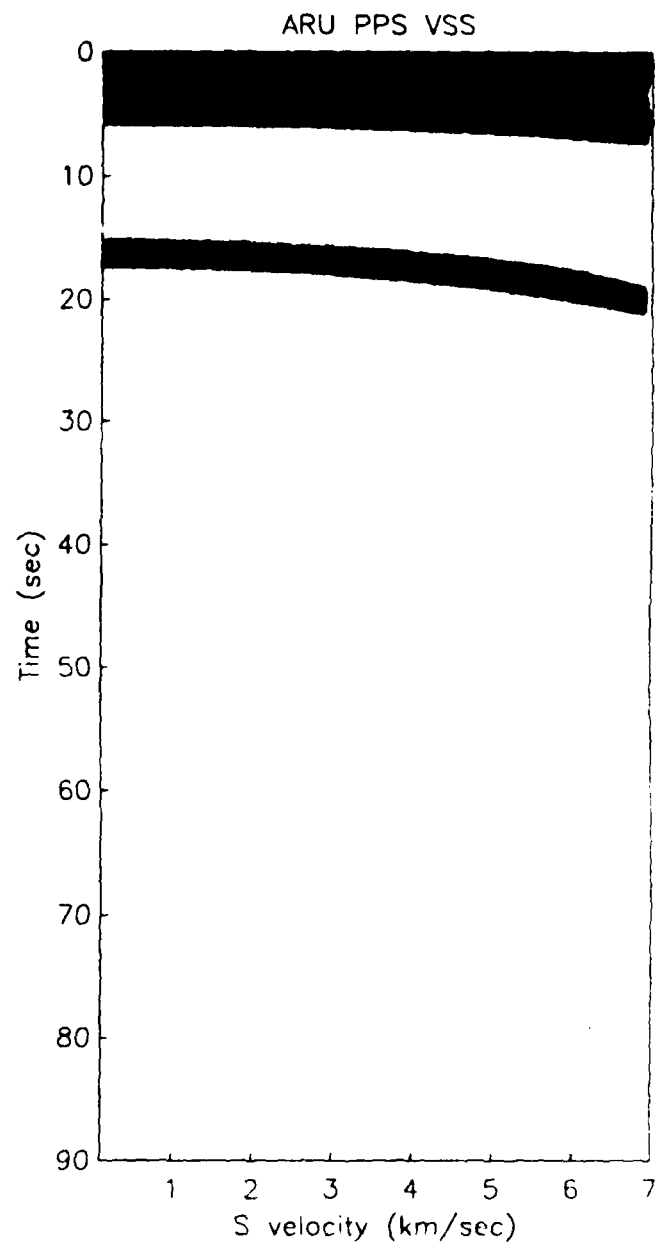
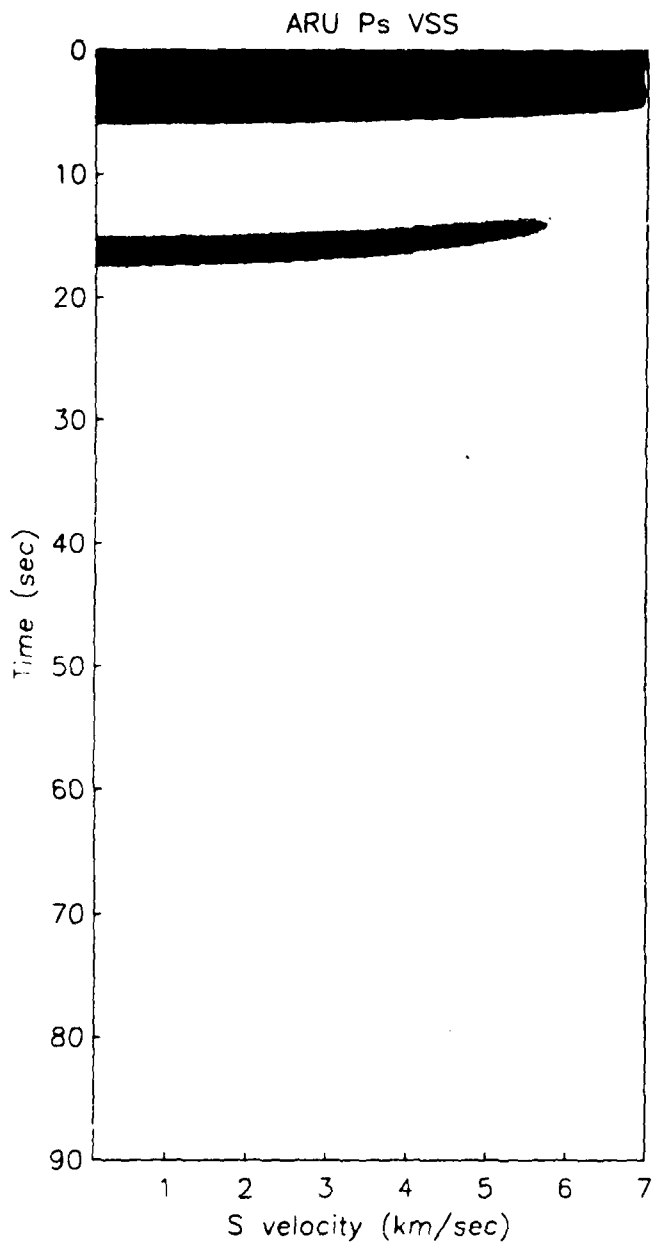


Figure 17. VSS_c computed from OBN receiver functions similar to that shown in Figure 15, except in this case, the VSS_c was computed using a value of 1.78 for R_v .



85 events $a=.6$ $v_p/v_s=1.825$

Figure 18. Velocity spectrum stacks produced from receiver functions computed from seismograms recorded at ARU. The plot on the left was computed for Ps phases while the one on the right was computed using the P2p1s moveout curve.

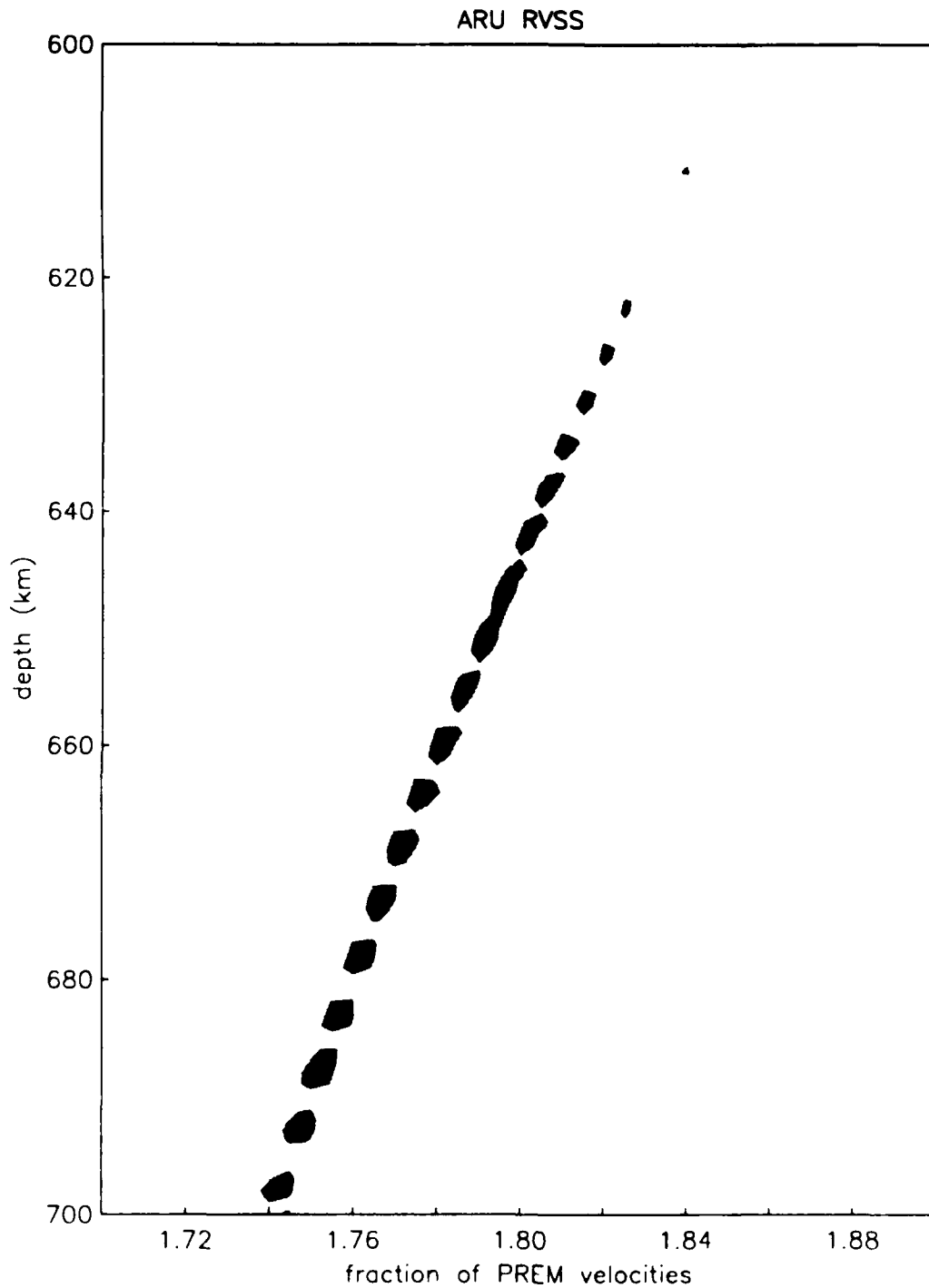


Figure 19. Velocity ratio spectrum stack (R_{vSS}) from the ARU receiver functions computed using PREM as the reference model.

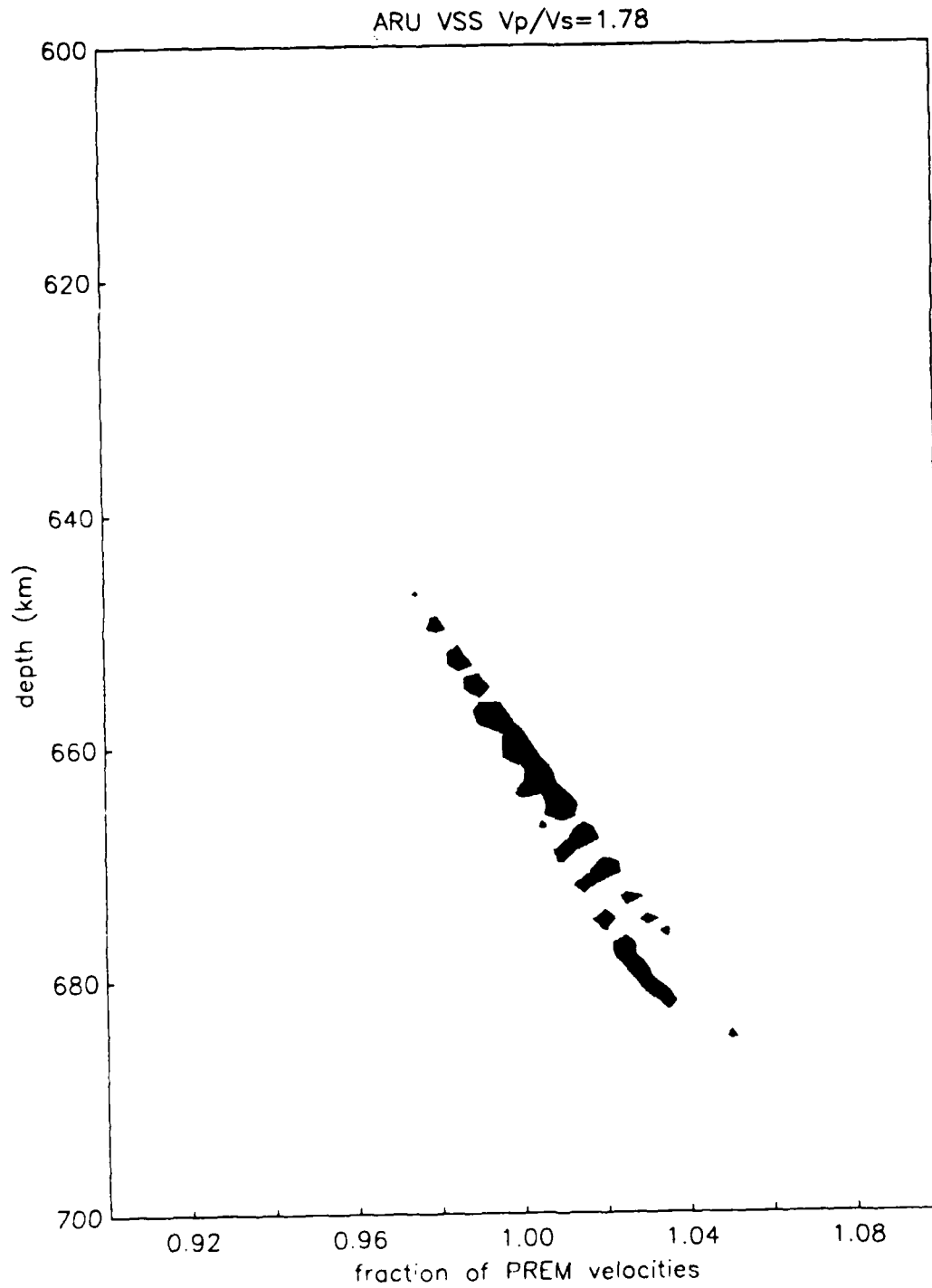


Figure 20. VSS_c computed from ARU receiver functions similar to that shown in Figure 19, except in this case, the VSS_c was computed using a value of 1.78 for R_v .

Prof. Thomas Ahrens
Seismological Lab, 252-21
Division of Geological & Planetary Sciences
California Institute of Technology
Pasadena, CA 91125

Prof. Keiiti Aki
Center for Earth Sciences
University of Southern California
University Park
Los Angeles, CA 90089-0741

Prof. Shelton Alexander
Geosciences Department
403 Deike Building
The Pennsylvania State University
University Park, PA 16802

Dr. Ralph Alewine, III
DARPA/NMRO
3701 North Fairfax Drive
Arlington, VA 22203-1714

Prof. Charles B. Archambeau
CIRES
University of Colorado
Boulder, CO 80309

Dr. Thomas C. Bache, Jr.
Science Applications Int'l Corp
10260 Campus Point Drive
San Diego, CA 92121 (2 copies)

Prof. Muawia Barazangi
Institute for the Study of the Continent
Cornell University
Ithaca, NY 14853

Dr. Jeff Barker
Department of Geological Sciences
State University of New York
at Binghamton
Vestal, NY 13901

Dr. Douglas R. Baumgardt
ENSCO, Inc
5400 Port Royal Road
Springfield, VA 22151-2388

Dr. Susan Beck
Department of Geosciences
Building #77
University of Arizona
Tucson, AZ 85721

Dr. T.J. Bennett
S-CUBED
A Division of Maxwell Laboratories
11800 Sunrise Valley Drive, Suite 1212
Reston, VA 22091

Dr. Robert Blandford
AFTAC/IT, Center for Seismic Studies
1300 North 17th Street
Suite 1450
Arlington, VA 22209-2308

Dr. Stephen Bratt
Center for Seismic Studies
1300 North 17th Street
Suite 1450
Arlington, VA 22209-2308

Dr. Lawrence Burdick
IGPP, A-025
Scripps Institute of Oceanography
University of California, San Diego
La Jolla, CA 92093

Dr. Robert Burrige
Schlumberger-Doll Research Center
Old Quarry Road
Ridgefield, CT 06877

Dr. Jerry Carter
Center for Seismic Studies
1300 North 17th Street
Suite 1450
Arlington, VA 22209-2308

Dr. Eric Chael
Division 9241
Sandia Laboratory
Albuquerque, NM 87185

Dr. Martin Chapman
Department of Geological Sciences
Virginia Polytechnical Institute
21044 Derring Hall
Blacksburg, VA 24061

Prof. Vernon F. Cormier
Department of Geology & Geophysics
U-45, Room 207
University of Connecticut
Storrs, CT 06268

Prof. Steven Day
Department of Geological Sciences
San Diego State University
San Diego, CA 92182

Marvin Denny
U.S. Department of Energy
Office of Arms Control
Washington, DC 20585

Dr. Cliff Frolich
Institute of Geophysics
8701 North Mopac
Austin, TX 78759

Dr. Zoltan Der
ENSCO, Inc.
5400 Port Royal Road
Springfield, VA 22151-2388

Dr. Holly Given
IGPP, A-025
Scripps Institute of Oceanography
University of California, San Diego
La Jolla, CA 92093

Prof. Adam Dziewonski
Hoffman Laboratory, Harvard University
Dept. of Earth Atmos. & Planetary Sciences
20 Oxford Street
Cambridge, MA 02138

Dr. Jeffrey W. Given
SAIC
10260 Campus Point Drive
San Diego, CA 92121

Prof. John Ebel
Department of Geology & Geophysics
Boston College
Chestnut Hill, MA 02167

Dr. Dale Glover
Defense Intelligence Agency
ATTN: ODT-1B
Washington, DC 20301

Eric Fielding
SNEE Hall
INSTOC
Cornell University
Ithaca, NY 14853

Dr. Indra Gupta
Teledyne Geotech
314 Montgomery Street
Alexandria, VA 22314

Dr. Mark D. Fisk
Mission Research Corporation
735 State Street
P.O. Drawer 719
Santa Barbara, CA 93102

Dan N. Hagedorn
Pacific Northwest Laboratories
Battelle Boulevard
Richland, WA 99352

Prof. Stanley Flatte
Applied Sciences Building
University of California, Santa Cruz
Santa Cruz, CA 95064

Dr. James Hannon
Lawrence Livermore National Laboratory
P.O. Box 808
L-205
Livermore, CA 94550

Dr. John Foley
NER-Geo Sciences
1100 Crown Colony Drive
Quincy, MA 02169

Dr. Roger Hansen
HQ AFTAC/TTR
130 South Highway A1A
Patrick AFB, FL 32925-3002

Prof. Donald Forsyth
Department of Geological Sciences
Brown University
Providence, RI 02912

Prof. David G. Harkrider
Seismological Laboratory
Division of Geological & Planetary Sciences
California Institute of Technology
Pasadena, CA 91125

Dr. Art Frankel
U.S. Geological Survey
922 National Center
Reston, VA 22092

Prof. Danny Harvey
CIRES
University of Colorado
Boulder, CO 80309

Prof. Donald V. Helmberger
Seismological Laboratory
Division of Geological & Planetary Sciences
California Institute of Technology
Pasadena, CA 91125

Prof. Eugene Herrin
Institute for the Study of Earth and Man
Geophysical Laboratory
Southern Methodist University
Dallas, TX 75275

Prof. Robert B. Herrmann
Department of Earth & Atmospheric Sciences
St. Louis University
St. Louis, MO 63156

Prof. Lane R. Johnson
Seismographic Station
University of California
Berkeley, CA 94720

Prof. Thomas H. Jordan
Department of Earth, Atmospheric &
Planetary Sciences
Massachusetts Institute of Technology
Cambridge, MA 02139

Prof. Alan Kafka
Department of Geology & Geophysics
Boston College
Chestnut Hill, MA 02167

Robert C. Kemerait
ENSCO, Inc.
445 Pineda Court
Melbourne, FL 32940

Dr. Karl Koch
Institute for the Study of Earth and Man
Geophysical Laboratory
Southern Methodist University
Dallas, Tx 75275

Dr. Max Koontz
U.S. Dept. of Energy/DP 5
Forrestal Building
1000 Independence Avenue
Washington, DC 20585

Dr. Richard LaCoss
MIT Lincoln Laboratory, M-200B
P.O. Box 73
Lexington, MA 02173-0073

Dr. Fred K. Lamb
University of Illinois at Urbana-Champaign
Department of Physics
1110 West Green Street
Urbana, IL 61801

Prof. Charles A. Langston
Geosciences Department
403 Deike Building
The Pennsylvania State University
University Park, PA 16802

Jim Lawson, Chief Geophysicist
Oklahoma Geological Survey
Oklahoma Geophysical Observatory
P.O. Box 8
Leonard, OK 74043-0008

Prof. Thorne Lay
Institute of Tectonics
Earth Science Board
University of California, Santa Cruz
Santa Cruz, CA 95064

Dr. William Leith
U.S. Geological Survey
Mail Stop 928
Reston, VA 22092

Mr. James F. Lewkowicz
Phillips Laboratory/GPEH
29 Randolph Road
Hanscom AFB, MA 01731-3010(2 copies)

Mr. Alfred Lieberman
ACDA/VI-OA State Department Building
Room 5726
320-21st Street, NW
Washington, DC 20451

Prof. L. Timothy Long
School of Geophysical Sciences
Georgia Institute of Technology
Atlanta, GA 30332

Dr. Randolph Martin, III
New England Research, Inc.
76 Olcott Drive
White River Junction, VT 05001

Dr. Robert Masse
Denver Federal Building
Box 25046, Mail Stop 967
Denver, CO 80225

Dr. Gary McCartor
Department of Physics
Southern Methodist University
Dallas, TX 75275

Prof. Thomas V. McEvelly
Seismographic Station
University of California
Berkeley, CA 94720

Dr. Art McGarr
U.S. Geological Survey
Mail Stop 977
U.S. Geological Survey
Menlo Park, CA 94025

Dr. Keith L. McLaughlin
S-CUBED
A Division of Maxwell Laboratory
P.O. Box 1620
La Jolla, CA 92038-1620

Stephen Miller & Dr. Alexander Florence
SRI International
333 Ravenswood Avenue
Box AF 116
Menlo Park, CA 94025-3493

Prof. Bernard Minster
IGPP, A-025
Scripps Institute of Oceanography
University of California, San Diego
La Jolla, CA 92093

Prof. Brian J. Mitchell
Department of Earth & Atmospheric Sciences
St. Louis University
St. Louis, MO 63156

Mr. Jack Murphy
S-CUBED
A Division of Maxwell Laboratory
11800 Sunrise Valley Drive, Suite 1212
Reston, VA 22091 (2 Copies)

Dr. Keith K. Nakanishi
Lawrence Livermore National Laboratory
L-025
P.O. Box 808
Livermore, CA 94550

Dr. Carl Newton
Los Alamos National Laboratory
P.O. Box 1663
Mail Stop C335, Group ESS-3
Los Alamos, NM 87545

Dr. Bao Nguyen
HQ AFTAC/TTR
130 South Highway A1A
Patrick AFB, FL 32925-3002

Prof. John A. Orcutt
IGPP, A-025
Scripps Institute of Oceanography
University of California, San Diego
La Jolla, CA 92093

Prof. Jeffrey Park
Kline Geology Laboratory
P.O. Box 6666
New Haven, CT 06511-8130

Dr. Howard Patton
Lawrence Livermore National Laboratory
L-025
P.O. Box 808
Livermore, CA 94550

Dr. Frank Pilotte
HQ AFTAC/TT
130 South Highway A1A
Patrick AFB, FL 32925-3002

Dr. Jay J. Pulli
Radix Systems, Inc.
201 Perry Parkway
Gaithersburg, MD 20877

Dr. Robert Reinke
ATTN: FCTVTD
Field Command
Defense Nuclear Agency
Kirtland AFB, NM 87115

Prof. Paul G. Richards
Lamont-Doherty Geological Observatory
of Columbia University
Palisades, NY 10964

Mr. Wilmer Rivers
Teledyne Geotech
314 Montgomery Street
Alexandria, VA 22314

Dr. George Rothe
HQ AFTAC/TTR
130 South Highway A1A
Patrick AFB, FL 32925-3002

Dr. Alan S. Ryall, Jr.
DARPA/NMRO
3701 North Fairfax Drive
Arlington, VA 22209-1714

Dr. Richard Sailor
TASC, Inc.
55 Walkers Brook Drive
Reading, MA 01867

Prof. Charles G. Sammis
Center for Earth Sciences
University of Southern California
University Park
Los Angeles, CA 90089-0741

Prof. Christopher H. Scholz
Lamont-Doherty Geological Observatory
of Columbia University
Palisades, NY 10964

Dr. Susan Schwartz
Institute of Tectonics
1156 High Street
Santa Cruz, CA 95064

Secretary of the Air Force
(SAFRD)
Washington, DC 20330

Office of the Secretary of Defense
DDR&E
Washington, DC 20330

Thomas J. Sereno, Jr.
Science Application Int'l Corp.
10260 Campus Point Drive
San Diego, CA 92121

Dr. Michael Shore
Defense Nuclear Agency/SPSS
6801 Telegraph Road
Alexandria, VA 22310

Dr. Robert Shumway
University of California Davis
Division of Statistics
Davis, CA 95616

Dr. Matthew Sibol
Virginia Tech
Seismological Observatory
4044 Derring Hall
Blacksburg, VA 24061-0420

Prof. David G. Simpson
IRIS, Inc.
1616 North Fort Myer Drive
Suite 1050
Arlington, VA 22209

Donald L. Springer
Lawrence Livermore National Laboratory
L-025
P.O. Box 808
Livermore, CA 94550

Dr. Jeffrey Stevens
S-CUBED
A Division of Maxwell Laboratory
P.O. Box 1620
La Jolla, CA 92038-1620

Lt. Col. Jim Stobie
ATTN: AFOSR/NL
110 Duncan Avenue
Bolling AFB
Washington, DC 20332-0001

Prof. Brian Stump
Institute for the Study of Earth & Man
Geophysical Laboratory
Southern Methodist University
Dallas, TX 75275

Prof. Jeremiah Sullivan
University of Illinois at Urbana-Champaign
Department of Physics
1110 West Green Street
Urbana, IL 61801

Prof. L. Sykes
Lamont-Doherty Geological Observatory
of Columbia University
Palisades, NY 10964

Dr. David Taylor
ENSCO, Inc.
445 Pineda Court
Melbourne, FL 32940

Dr. Steven R. Taylor
Los Alamos National Laboratory
P.O. Box 1663
Mail Stop C335
Los Alamos, NM 87545

Prof. Clifford Thurber
University of Wisconsin-Madison
Department of Geology & Geophysics
1215 West Dayton Street
Madison, WI 53706

Prof. M. Nafi Toksoz
Earth Resources Lab
Massachusetts Institute of Technology
42 Carleton Street
Cambridge, MA 02142

Dr. Larry Turnbull
CIA-OSWR/NED
Washington, DC 20505

Dr. Gregory van der Vink
IRIS, Inc.
1616 North Fort Myer Drive
Suite 1050
Arlington, VA 22209

Dr. Karl Veith
EG&G
5211 Auth Road
Suite 240
Suitland, MD 20746

Prof. Terry C. Wallace
Department of Geosciences
Building #77
University of Arizona
Tucson, AZ 85721

Dr. Thomas Weaver
Los Alamos National Laboratory
P.O. Box 1663
Mail Stop C335
Los Alamos, NM 87545

Dr. William Wortman
Mission Research Corporation
8560 Cinderbed Road
Suite 700
Newington, VA 22122

Prof. Francis T. Wu
Department of Geological Sciences
State University of New York
at Binghamton
Vestal, NY 13901

AFTAC/CA
(STINFO)
Patrick AFB, FL 32925-6001

DARPA/PM
3701 North Fairfax Drive
Arlington, VA 22203-1714

DARPA/RMO/RETRIEVAL
3701 North Fairfax Drive
Arlington, VA 22203-1714

DARPA/RMO/SECURITY OFFICE
3701 North Fairfax Drive
Arlington, VA 22203-1714

HQ DNA
ATTN: Technical Library
Washington, DC 20305

Defense Intelligence Agency
Directorate for Scientific & Technical Intelligence
ATTN: DTIB
Washington, DC 20340-6158

Defense Technical Information Center
Cameron Station
Alexandria, VA 22314 (2 Copies)

TACTEC
Battelle Memorial Institute
505 King Avenue
Columbus, OH 43201 (Final Report)

Phillips Laboratory
ATTN: XPG
29 Randolph Road
Hanscom AFB, MA 01731-3010

Phillips Laboratory
ATTN: GPE
29 Randolph Road
Hanscom AFB, MA 01731-3010

Phillips Laboratory
ATTN: TSML
5 Wright Street
Hanscom AFB, MA 01731-3004

Phillips Laboratory
ATTN: PL/SUL
3550 Aberdeen Ave SE
Kirtland, NM 87117-5776 (2 copies)

Dr. Svein Mykkeltveit
NTNT/NORSAR
P.O. Box 51
N-2007 Kjeller, NORWAY (3 Copies)

Dr. Michel Bouchon
I.R.I.G.M.-B.P. 68
38402 St. Martin D'Herès
Cedex, FRANCE

Prof. Keith Priestley
University of Cambridge
Bullard Labs, Dept. of Earth Sciences
Madingley Rise, Madingley Road
Cambridge CB3 0EZ, ENGLAND

Dr. Michel Campillo
Observatoire de Grenoble
I.R.I.G.M.-B.P. 53
38041 Grenoble, FRANCE

Dr. Jorg Schlittenhardt
Federal Institute for Geosciences & Nat'l Res.
Postfach 510153
D-3000 Hannover 51, GERMANY

Dr. Kin Yip Chun
Geophysics Division
Physics Department
University of Toronto
Ontario, CANADA

Dr. Johannes Schweitzer
Institute of Geophysics
Ruhr University/Bochum
P.O. Box 1102148
4360 Bochum 1, GERMANY

Prof. Hans-Peter Harjes
Institute for Geophysics
Ruhr University/Bochum
P.O. Box 102148
4630 Bochum 1, GERMANY

Trust & Verify
VERTIC
8 John Adam Street
London WC2N 6EZ, ENGLAND

Prof. Eystein Husebye
NTNF/NORSAR
P.O. Box 51
N-2007 Kjeller, NORWAY

David Jepsen
Acting Head, Nuclear Monitoring Section
Bureau of Mineral Resources
Geology and Geophysics
G.P.O. Box 378, Canberra, AUSTRALIA

Ms. Eva Johannisson
Senior Research Officer
FOA
S-172 90 Sundbyberg, SWEDEN

Dr. Peter Marshall
Procurement Executive
Ministry of Defense
Blacknest, Brimpton
Reading FG7-FRS, UNITED KINGDOM

Dr. Bernard Massinon, Dr. Pierre Mechler
Societe Radiomana
27 rue Claude Bernard
75005 Paris, FRANCE (2 Copies)